UNIVERSITY OF PITTSBURGH

Study of Intermediate Oxidation Products in Chemical and Enzymatic Degradation of Carbon Nanomaterials

by

Hao Bai

B. S. in Chemistry, Peking University, 2006

Submitted to the Graduate Faculty of

The Kenneth P. Dietrich School of Arts and Sciences in partial fulfillment

of the requirements for the degree of

Master of Science

University of Pittsburgh

2013

UNIVERSITY OF PITTSBURGH

THE KENNETH P. DIETRICH SCHOOL OF ARTS AND SCIENCES

This thesis was presented

by

Hao Bai

It was defended on

December 9th, 2012

and approved by

Renã A. S. Robinson, Assistant Professor, Department of Chemistry

Haitao Liu, Assistant Professor, Department of Chemistry

Thesis Advisor: Alexander Star, Associate Professor, Department of Chemistry

Study of Intermediate Oxidation Products in Chemical and Enzymatic Degradation of Carbon Nanomaterials

Hao Bai, M.S.

University of Pittsburgh, 2013

With increasing applications of carbon nanomaterials, toxicity of the material itself and its degradation products in both biological systems and the environment becomes a valid concern. At present, most of the toxicity studies only focus on the bulk properties of carbon nanomaterials and the relevant conclusions are ambiguous. To better understand the degradation mechanism and potential sources of toxicity, we separated the oxidation products, which consisted of "small molecules" and "large particles", and studied these compounds/materials in detail. In the first oxidation method, graphene oxide was degraded by Fenton reagent ($Fe^{2+}/Fe^{3+}/H_2O_2$) under UV irradiation. Using analytical techniques that included mass spectrometry (MS), nuclear magnetic resonance (NMR) and liquid chromatography (LC), we successfully proposed plausible structures for degradation products and discovered several structure patterns. Also, by using atomic force microscopy (AFM) and spectrofluorometry, we monitored the morphological transformation of graphene oxide flakes (~ 600 nm × 1 nm) to graphene quantum dots (~ 25 nm × 5 nm), both in aqueous solution and immobilized on a substrate. Given the similarity of Fenton reagent chemical oxidation and myeloperoxidase (MPO) enzymatic degradation of carbon nanomaterials, our results will not only help to elucidate the enzymatic degradation mechanism *in vivo* and in the environment, but also to assess the nanomaterial toxicity at different stages of the degradation process. In the second part, we studied the degradation of SWNTs in both MPO and NaClO systems; the MS data obtained from these experiments were limited by the ion suppression resulting from the high salt concentrations.

TABLE OF CONTENTS

LIST OF FIGURES vii

LIST OF EQUATIONS ix

ABRREVIATIONS x

1. INTRODUCTION 1

  1.1. Overview 1

  1.2. Synthesis of Graphene 2

  1.3. Carbon Nanotubes 4

  1.4. Photo Fenton Reaction 8

  1.5. Enzymatic degradation and chemical oxidation of carbon nanomaterials 10

  1.6. Analytical Technique Introduction 12

    1.6.1. Liquid Chromatography 12

    1.6.2. Mass Spectrometry 15

    1.6.3. Nuclear Magnetic Resonance 19

2. RESEARCH PROGRESS 20

  2.1. ESI-MS of Standard Compounds 20

  2.2. General Rules for Tentative Structure Proposal 22

  2.3. Photo Fenton Reaction of Graphene Oxide and Product Characterization 24

    2.3.1. Experimental 24

    2.3.2. Results and Discussion 27

  2.4. Identification of Degradation Products in MPO and NaClO system 43

    2.4.1. Experimental 43

2.4.2. Results and Discussion 47

2.4.2.1. Chemical Degradation of SWNTs with NaClO at High Temperature 47

3. CONCLUSION AND FUTURE PLANS 59

3.1. Degradation Mechanism Elucidation 59

3.2. Toxicity of Degradation Products Study based on the Identified Products in Different Systems 60

4. BIBLIOGRAPHY 61

LIST OF FIGURES

Figure 1. Carbon Nanomaterials 1

Figure 2. Synthesis of Graphene 2

Figure 3. Carbon Nanotubes 4

Figure 4. Classification of SWNTs 7

Figure 5. Schematic of HPLC instrument. 12

Figure 6. Schematic of electrospray ionization process 17

Figure 7. Schematic of matrix-assisted laser desorption ionization 17

Figure 8. Schematic of Electrospray ionization mass spectrometry (ESI-MS) utilized. 18

Figure 9. Oxygen containing functional groups 20

Figure 10. Characterization of Graphene Oxide 29

Figure 11. Mass spectrum of GO degradation products 31

Figure 12. Proposed structures 34

Figure 13. Tandem MS 34

Figure 14. NMR spectra 37

Figure 15. On-chip AFM images of Graphene Oxide Oxidation 38

Figure 16. Height profile of GO Oxidation at early stage 39

Figure 17. Section Analysis GO Oxidation 41

Figure 18. AFM images of control experiment (I) 42

Figure 19. AFM images of control experiment (II) 42

Figure 20. Characterization of SWNTs 48

Figure 21. Raman spectra of SWNTs during NaClO oxidation 49

Figure 22. Separation of Oxidation Products 51

Figure 23. Comparison of MS spectra of oxidation products of SWNTs in NaClO oxidation 53

Figure 24. Chip design 54

Figure 25. Monitor the evolution of MPO enzymatic degradation by AFM 57

Figure 26. Height profile of SWNTs during MPO enzymatic degradation 58

LIST OF EQUATIONS

Equation 1. Mechanism of Fenton Reaction..8

Equation 2. Mechanism of Photo Fenton Reaction 8

ABRREVIATIONS

AFM	Atomic Force Microscopy
CNTs	Carbon Nanotubes
CVD	Chemical Vapor Deposition
ESI	Electrospray Ionization
GO	Graphene Oxide
LC-MS	Liquid Chromatography- Mass Spectrometry
MWCNTs	Multi-Walled Carbon Nanotubes
SWCNTs	Single-Walled Carbon Nanotubes
TEM	Transmission Electron Microscopy

1. INTRODUCTION

1.1. Overview

Carbon is regarded as the "chemical genius"[1] for its ability to bond in different ways, adopting different hybridizations of four valence orbitals, and to create various allotropes with entirely different properties. When sp^3 hybridization is adopted, isotropical bonding leads to stable and firm structure as in diamond, while the sp^2 hybridization will form a layered structure with strong in-plane bond and weak out-of-plane interaction, as in graphite.[2] Tremendous endeavors are devoted to the development and production of new type of allotropes of carbon and carbon nanomaterials, such as fullerene[3], graphene and carbon nanotubes (CNTs), become the focus of many researches.

Graphene, the parent of all graphitic forms,[4] is a two-dimensional sheet of sp^2 hybridized carbon. On one hand, it can be stacked to form graphite, folded to from 1D nanotubes, and wrapped to form 0D fullerenes (Figure 1), on the other hand, different from those carbon allotropes, the long

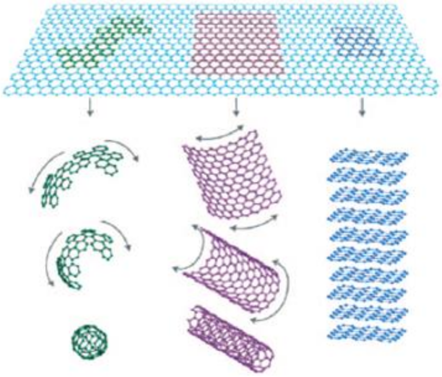

Figure 1. Carbon Nanomaterials
Schematic illustration of the transformation from graphene to fullerene, SWNT and graphite; adopted from Ref. 4.

range π-conjugation in graphene leads to unique thermal, mechanical and electrical properties.

1.2. Synthesis of Graphene

Not only is the single-layer graphene investigated, but the bi-layer and few-layer graphenes attract considerable interest as well. The synthesis and characterizations considering different forms of graphenes are investigated and various progresses were made to produce large scale and controllable form of graphene. Ruoff's group,[5] for the first time, demonstrated a solution-based process to produce single-layer graphene, which is shown in Figure 2. In this low cost approach, graphitic oxide is mechanically or thermally exfoliated to produce single-layer graphene oxide (GO) via Hummer's method[6]. Then GO is reduced by hydrazine or other reducing agents to give reduced single-layer graphene (RGO). More methods were developed to reduce GO to RGO, chemically or thermally. Bi-layer and few-layer graphenes also have been synthesized with other methods. [7-9]

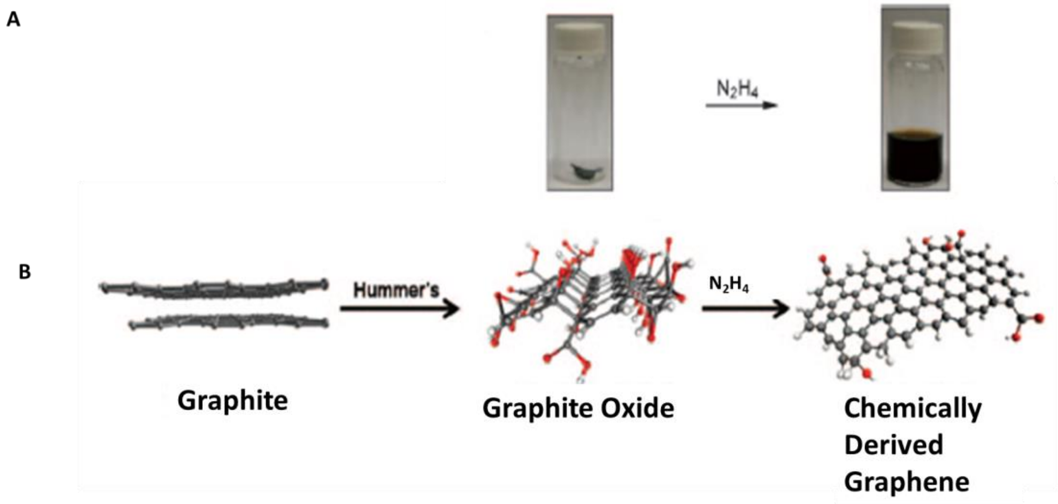

Figure 2. Synthesis of Graphene
(A) Photographs showing the conversion of graphite oxide in the vial (left) to the reduced graphene dispersion after addition of hydrazine. (B) Molecular models showing the conversion from graphite to graphene (C gray, O red, H white); adopted from ref. 6.

Another method to synthetize graphene is the thermal decomposition of silicon carbide under ultrahigh vacuum, allowing graphitic films to be grown epitaxially.[10,11] During the process, SiC is heated to high temperature (> 1000 ^{o}C) and Si will sublimate, leaving small islands of graphene and producing ultrathin graphene sheets. The layer thickness, typically 1 – 3 layers, is predominantly determined by temperature.

Chemical vapor deposition (CVD) on transition metal films is another bottom-up approach to synthesize high quality monolayer and multilayer graphene. Extensive researches has been done to study epitaxial growth of graphene on metal substrates, such as Co[12], Pt[13] and Ir[14] , however the graphene synthesized was of poor quality in terms of uniformity. In 2009, Kong and the coworkers[15] demonstrated the graphene growth on polycrystalline Ni films via CVD. During the process, Ni film was exposed to a diluted hydrocarbon flow under ambient pressure, producing ultrathin graphene film (1 to ~ 10 layers). The produced film is mainly single-layer graphene with satisfactory uniformity. In the same year, Ruoff and coworkers[5] reported the growth of large area graphene (centimeters) on copper foil using methane via CVD. After the synthesis, the metal can be easily removed and the graphene film can be transferred to arbitrary substrates for further application.

To sum up, mainly four methods have been developed for graphene synthesis, including exfoliation from graphite, reduction from graphene oxide, epitaxial growth on silicon carbide and CVD. Graphene synthesized from different methods can have various properties, and choice can be made according to the specific application aspect.

1.3. Carbon Nanotubes

Since their discovery,[16,17] CNTs have been the focus of considerable research. This unique one-dimensional nanometer-scale material imparts exceptionally high mechanical strength, high resilience, and electronic properties changing from metallic to semiconducting and high thermal conductivity. According to the number of graphitic walls, CNTs can be divided into single-walled nanotubes (SWNTs) (Figure 3A) and multi-walled nanotubes (MWNTs) (Figure 3B).

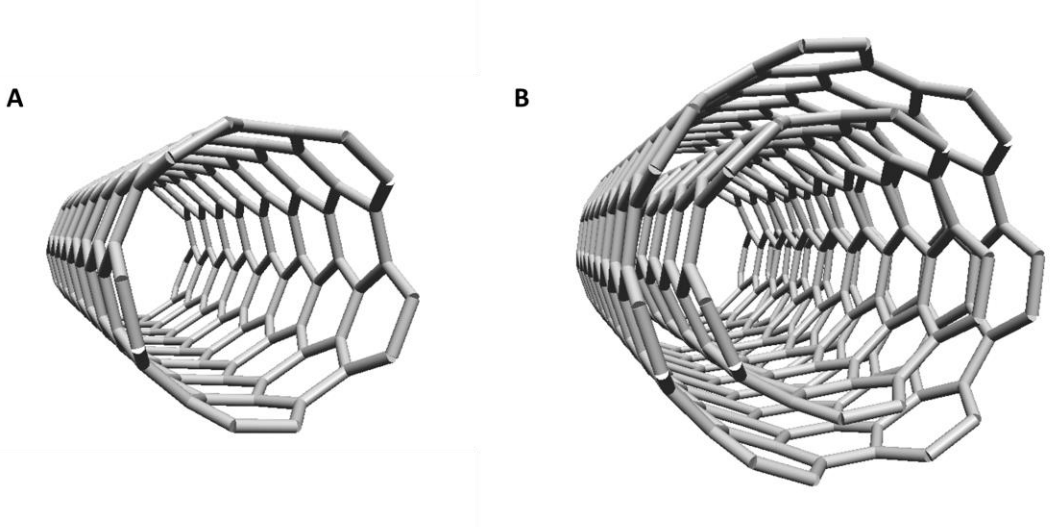

Figure 3. Carbon Nanotubes
(A) Morphological illustration of single-walled nanotube (SWNT) and (B) multi-walled carbon nanotube (MWNT).

Currently, single- or multi-walled CNTs are mainly synthesized by the following three techniques: electric arc-discharge, laser vaporization of graphite targets and chemical vapor deposition (CVD).

In electric arc-discharge, a direct current (80 – 100 A) through two high-purity graphite (6 – 10 mm OD) electrodes separated by 1 – 2 mm is applied, in a He atmosphere (500 torr).[18] During arcing, carbon deposit forms on the cathode (negative electrode), which consists of randomly arranged MWNTs. Metal catalyst is introduced in the process to obtain SWNTs. The first reported synthesis of SWNTs by Iijima and Ichihashi[19] was produced by arcing Fe-graphite electrodes in a methane-argon atmosphere. More metal catalysts, such as Gd[20], Co-Pt,[21] Co-Ru,[21] Co,[22] Ni-Y,[23] Rh-Pt,[24] and Co-Ni-Fe-Ce,[25] have been developed since then. However, the production cost is high since the procedure requires high purity of graphite electrodes and metal catalyst and gas atmosphere. In addition, the dimension of the tubes is not well controlled. Besides, by-products, such as polyhedral graphite particles, encapsulated metal particles and amorphous carbon, are formed.

For laser ablation or laser vaporization of graphite targets, MWNTs are generated by the high-power laser evaporation of the pure graphite targets at 1200 ℃ in an Ar atmosphere.[26] The nanotubes could be collected from a Cu-cooled water trap. To synthetize SWNTs, metal catalyst, such as Co-Ni, is also needed.[27] However, this method is still not economically viable. Besides, the yield is lower than that of the electric arc-discharge method.

CVD is a common method for the large scale commercial synthesis of carbon nanotubes. During CVD, the layer of metal catalyst particles, like Ni, Co,[28] Fe or alloy,[29] are prepared on top of the substrate by reduction of the oxides or oxides solid solutions. The substrate is heated to certain temperature (700 to 1200 ℃) in the quartz tube, with the presence of H_2 and hydrocarbon gas (like CH_4 and C_2H_4). Hydrocarbon molecules decompose on the surface of the catalyst particle and the carbon atoms diffuse to the edges of the catalyst particle, resulting in the formation of the carbon nanotubes. The diameters of the nanotubes are closely related to the size of the catalyst particles. The mechanism between the pyrolysis step and the tube formation is still under debate.[30] At present, the following mechanisms have been widely proposed:

a) Top carbon diffusion through catalytic particles: After decomposition of hydrocarbon on the top surfaces of the metal catalyst particles, the carbon fragments diffuse through the particle and precipitate at the cooler side on the other end of the catalyst particle, resulting in the growth of nanotube underneath the catalyst particle.[31,32]

b) Bottom carbon diffusion through catalytic particles: Nanotube growth occurs due to the rapid movement of carbon species through the catalyst by diffusion, thus segregating the nanotube.[33,34] Unlike the mechanism above, nanotubes grow from their bases rather than their tips.

To understand the electronic properties of SWNTs, one could start with folding a sheet of graphene into a perfect matched cylinder, which will result in an open ended tube (Figure 4). When seaming the two sides of the graphene, there are multiple ways to combine the elements from the edges, resulting in various helical properties. Theoretically, when satisfying the Bravais lattice vectors, the line along which the graphene is folded is characterized by vector $R=ma_1+na_2$ and nanotubes made from indices of (n, 0), (n, m) or any number between these two will have different symmetrical operations, determining the electric properties and chirality of nanotubes. To be more specific, when $|n-m|=3q$, where q is an integer, the nanotubes are metallic and otherwise semiconducting. The (n, 0) type of nanotubes is generally called zigzag and (n, n) armchair; all the others are called chiral. MWNTs are made of concentric SWNTs and typical diameter can range from several to tens of nanometers. The interlayer spacing between the adjacent layers is 0.34 nm. Different from SWNTs, the MWNTs are all metallic with zero band gaps.

The unique characteristics of SWNTs offer various opportunities for wide range of applications

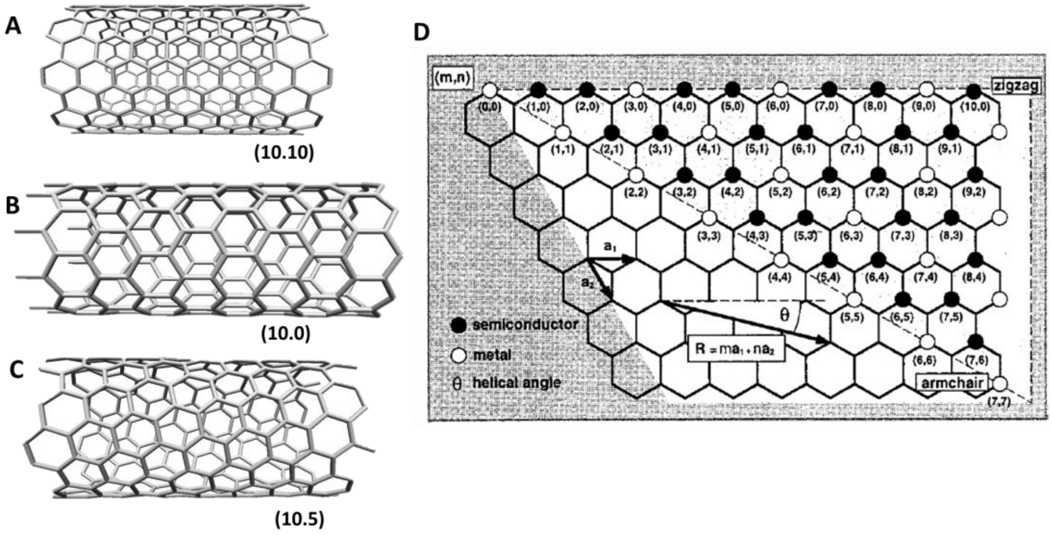

Figure 4. Classification of SWNTs

(A)-(C) Schematic of the basic unit of a SWNT with different folding indices as labeled under the nanotube. The cylindrical structure is constructed from graphene sheet of sp^2 bonded carbon with no dangling bonds. (D) Indexing scheme of folding planar graphene sheets to cylinders. $\mathbf{a_1}$ and $\mathbf{a_2}$ are primitive lattice vectors of the hexagonal lattice, adopted from Ref.1. The (n,n) type nanotube will form armchair tubes shown in (A) and all (n, 0) tubes are zigzag tubes shown in (B).

such as in composite materials,[35] chemical sensing[36,37] and drug delivery.[38] Since synthetic chemistry and biological processes primarily take place in solution phase, dissolution process of the as-prepared SWNTs (AP-SWNTs) is required in most cases. Modifications, including covalent functionality[38] such as oxidation[39] and non-covalent functionalization with surfactants[40] or bioconjugates [35], were applied not only to increase the solubility of nanotubes, but also to improve nanotube properties such as reinforced mechanical strength,[41] biocompatibility[38] and electrochemical sensitivity.

1.4. Photo Fenton Reaction

Since the invention of Fenton reagent in 1894 by Henry Fenton,[42] the relatively simple and straightforward reaction named after him was studied systematically[42-44] and developed from various aspects[44-50] and applied in numerous situations, [44,45]especially in wastewater treatment, in dealing with Polycyclic Aromatic Hydrocarbons (PAH).[22,23] The oxidation mechanism was well-elucidated although still debated. The generally accepted mechanism is as following:[44]

$$Fe^{2+} + H_2O_2 \rightarrow Fe^{3+} + OH^- + OH^\bullet (1)$$
$$Fe^{3+} + H_2O_2 \rightarrow Fe^{2+} + OOH^\bullet + H^+ (2)$$

Equation 1. Mechanism of Fenton Reaction

Usually, the radicals, especially the hydroxyl ($OH^\bullet$) radicals, initiate the reaction and lead to the oxidation of organic compounds. Although the reaction is simple, there are still some disadvantages. First, the reaction is relative slow. Second, even though the concentration of Fe^{2+} is low (50-80 ppm), it is still much higher than some standards, such as European Community Directives (2 ppm), in some occasions[50]. Third, the storage and transport of H_2O_2 might be dangerous. Accordingly, various endeavors were dedicated to improving the system. With the introduction of UV radiation[44], in so-called Photo-Fenton reaction, the reaction rates can be accelerated to a large extent. As discussed above in equation (1), $OH^\bullet$ radicals were first generated in the system. With the radiation, the reaction chain will implement anther path from Fe^{3+} to Fe^{2+}:

$$Fe^{3+} + H_2O_2 + hv \rightarrow Fe^{2+} + OH^\bullet + H^+ (3)$$

Equation 2. Mechanism of Photo Fenton Reaction

As a result, the Photo-Fenton reaction produces additional $OH^{\bullet}$ and accelerates the recycling of Fe^{2+} catalyst.[44] For the potential problems caused by H_2O_2 handling, Electro-Fenton oxidation system introduces the photoelectrocatalytic oxidation[51-53], in which H_2O_2 was generated continuously at the cathode made of inert materials and no addition of H_2O_2 is necessary to initiate the oxidation[53]. To further reduce the concentration of Fe^{2+}, heterogeneous Fenton Reaction[46] is a feasible choice.

Recently, Fenton Reaction and its improved variations were introduced for degradation of carbon nanotubes[54] and GO[55]. This approach attracts researchers for various reasons. First, the reaction is efficient, effective and economical. For example, Zhou. et al. demonstrated that graphene oxide could be cut into ~4 nm quantum dots in 15 mins[55] with a 1000W UV radiation. Second, the system is relatively simple compared with other carbon nanomaterial degradation systems, with low concentration of salt, which turns out to be instrument friendly, especially for MS spectrometry and chromatography. Furthermore, the Fenton Reaction of carbon nanomaterials may undertake similar oxidation process as that of biodegradation systems, such as peroxidases. Elucidation of the mechanism for the degradation of carbon nanomaterials by Fenton Reaction can be helpful for understanding of enzymatic biodegradation system.

In Zhou’s paper[55], the authors demonstrated the effective and efficient oxidation of graphene oxide with Photo-Fenton reaction in 15 mins with UV exposure. In my research, similar reaction was performed. Different from their work, our focus was on the identification of small degradation products, using mainly MS, LC-MS and NMR. Based on the products’ structures, degradation mechanism can be proposed, which can help to a large extent to understand the biodegradation process.

1.5. Enzymatic degradation and chemical oxidation of carbon nanomaterials

In recent years, unique physicochemical characteristics of carbon nanomaterials lead to a wide variety of applications in various fields of industry as well as in biotechnology and medicine.[36,37,56] Meanwhile, concerns aroused of the potential toxicity of these materials and their degradation products[57-60]. A few investigations were conducted on the degradation and elimination of carbon nanomaterials, especially SWNTs[61-64], and possible degradation mechanisms were proposed based on the results of routine characterization methods. Both chemical and enzymatic methods were developed for degradation of carbon nanomaterials, including SWNTs,[62 64,65]MWNTs[66] and graphene[67,68].

Among the chemical methods, a common procedure for modification and degradation of SWNTs was their treatment with acids, including piranha solution (mixture of 30% hydrogen peroxide and sulfuric acid at ratio of 1:3), H_2SO_4/HNO_3 and $HCl/H_2SO_{4.}$[63,69] Such oxidation can introduce oxygen containing functional groups including carbonyl and hydroxyl on the surface of SWNTs, thus creating defects and resulting in the breaking and shortening of SWNTs. Although acid treatment is simple and efficient, it cannot be applied for SWNT degradation in vivo and in the environment. More biocompatible systems were needed to realize the elimination of SWNTs in these settings.

As was recently demonstrated by our group[37,] biodegradation of SWNTs with horseradish peroxidase (HRP) and hydrogen peroxide can be observed over the period of several weeks. Characterization of SWNTs using microscopy and spectroscopy methods was done to monitor and confirm the process of the enzymatic degradation. However, the plant-derived enzyme is only relevant to SWNT degradation by biological systems in the environment. The further research target would be the development of biodegradation in animal body, especially in mammals.

In mammals, the major peroxidase is myeloperoxidase (MPO), which is present in immune cells such as neutrophils and macrophages. In the following research in our group and collaborators[43], biodegradation of SWNTs with MPO was demonstrated both in vitro and in vivo. Moreover, no inflammation was found in the lungs of mice with injection of biodegraded nanotubes[41]. This research and other studies[64] pointed out that the observed ability to biodegrade SWNTs was resulting from, most importantly, the generation of hypochlorite from MPO, free radicals created from heme degradation and active oxoferryl intermediates. As a result, a logical assumption can be made that the degradation products of SWNTs could be similar for enzymatic degradation with MPO and chemical degradation with hypochlorite. The latter is relatively simple oxidation system, which was previously studied and described in several publications.[70,71].

In my research, both MPO and NaClO systems were studied. Previously, to fully understand the degradation/oxidation mechanism of SWNTs, various analytical characterization methods were routinely used[64,65,70,72], including transmission electron microscopy (TEM), scanning electron microscopy (SEM) , Raman and thermal gravimetric analysis (TGA). These methods, however, can provide information only about the relatively large degradation products, while the small molecules are usually neglected. To overcome this limitation, I applied additional analytical techniques, including high-performance liquid chromatography (HPLC), ultraviolet-visible absorption spectroscopy (UV-Vis), mass spectrometry (MS) and nuclear magnetic resonance spectroscopy (NMR), to identify all the compounds formed in the degradation process. By combining and analyzing the data, possible structures were proposed.

1.6. Analytical Technique Introduction

1.6.1. Liquid Chromatography

Chromatography, meaning “color writing” in Greek, was first employed by Russian scientist Mikhail Tsvet in 1900, for the separation of plant pigments with different colors.[73] With the work of Archer John Porter Martin and Richard Laurence Millington Synge during the 1940s and 1950s,[74] several chromatographic methods, including paper chromatography, gas chromatography and high performance liquid chromatography (HPLC), were developed.[75] The basic principle for chromatography is a separation process in which the sample mixture is distributed between two phases, stationary and mobile phase, in the chromatographic bed (column or plane). The stationary phase is either a solid, porous, surface-active material in small-particle form or a thin film of liquid coated on a solid support or column wall.[76] The mobile phase is a gas or liquid. If liquid is used, the process is known as liquid chromatography.

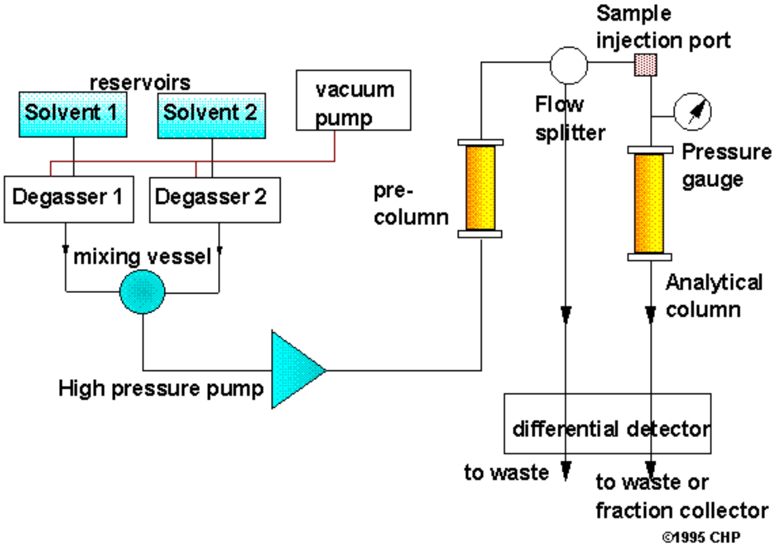

Figure 5. Schematic of HPLC instrument, adopted from ref 74.

Figure 5 illustrates the typical set up of HPLC instrument.[77] It usually consists of reservoirs of mobile phases, pumps, sample injector, column and detector and sometimes a pre-column is applied to diminish the potential damage of the sample to the column. When the sample mixture passes through the column, different components in the mixture will flow at different rates due to differences in their partitioning behavior between the stationary phase and mobile phase.

HPLC can be divided into multiple sub-classes based on different separation modes,[76,78] including adsorption chromatography (also known as normal phase chromatography), reversed phase liquid chromatography, (RPLC), ion exchange chromatography, ion pair chromatography, ion chromatography, size exclusion chromatography and affinity chromatography. In normal phase liquid chromatography, a relatively polar material, such as silica, is used as the stationary phase and relatively nonpolar solvent, such as heptane, is used as mobile phase. As a result, the polar compounds are eluted later than the nonpolar compounds. In RPLC, the reverse of the above applies: stationary phase is nonpolar while the mobile phase is relatively polar, such as water, and polar compounds elute faster than less polar compounds. One of the most important chromatography for ion separation is ion exchange chromatography. [79] The stationary phase usually contains ionic groups, such as NR_3^+ and SO_3^-, which interact with the ionic groups of the sample. If the stationary phase has fixed positive ions, then the exchangeable ions will be anionic and the anion exchange will be conducted. To the opposite, if stationary phase has fixed negative ions, then the mechanism will be cation exchange.

The detector is used to recognize when a substance zone is eluted from the column and quantitatively represent the amount the eluted compound.[76] Selectivity, noise, detection limit, linear range and time constant are all important factors to consider when picking a detector.

Typically,[76] UV detector,[78] refractive index detector, fluorescence detector, electrochemical detectors,[80] and light scattering detectors. Over the past decade, with the development of mass spectrometry, the combination of LC and MS (LC/MS) is increasingly important, with powerful features for the structure, qualitative and quantitative analysis[81-83].

1.6.2. Mass Spectrometry

Mass spectrometry (MS)[84], dealing with mostly the gaseous ionic state, measures the mass-to-charge ratio of charged particles. It is widely applied to determine mass of particle and elemental composition and to elucidate the chemical structure of molecules. The three essential components of MS include *the ion source*, where the sample is ionized, *the mass analyzer*, where the ions are sorted and separated according to the mass to charge ratio, and *the detector*, where the separated ions are measured.

Driven by the force to ionize and record the mass spectra of thermally unstable[84], nonvolatile compounds of biological sample and of increasing molecular weight, a breakthrough was made with the introduction of electrospray (ESI) and matrix-assisted laser desorption ionization (MALDI) for the ionization of unstable and nonvolatile molecules, especially the biological molecules. Figure 6[85] illustrates the schematic of typical electrospray ionization process. The solution is pumped through a capillary and produce charged droplets at the capillary tip. A high voltage (2-5 kV), either negative or positive according to specific situation, is applied to the capillary. Under the electric field, the charged droplets will shrink by solvent evaporation and repeatedly disintegrate into very small highly charged droplets, which then produce gas phase ions. Various theories have been proposed about the mechanism of gas phase ion production. Then the vapor phase ions can be analyzed within the mass analyzer. One important factor that can affect the performance of ESI is ion suppression, mainly caused by nonvolatile (e.g. salts) or less volatile solvent. The nonvolatile compounds can decrease the efficiency of droplet formation or droplet evaporation, which in turn affects the amount of charged ion in the gas phase that ultimately reaches the detector. The presence of ion suppression makes the desalination and purification of the sample necessary. Figure 7 [86] illustrates the schematic of MALDI. Although there is ongoing discussion about the primary ion formation, MALDI is generally accepted as a two-step process: desorption and ionization. First, under the laser beam, the matrix material can absorb energy, convert it mostly to heat and evaporate. The hot plume contains many species, including matrix molecules, analytes, and protonated and deprotonated matrix molecules, and nanodroplets. Then the analytes molecules are ionized in the hot plume, during which the collision is essential. After ionization, the analyte ions are drawn by the voltage applied across the chamber to mass analyzer. Different from DSI, the ion suppression in MALDI is tolerable, while in lower mass to charge ration region, the matrix suppression can be dominant. The ionization can be affected by the matrix and laser energy.

In my research, an LTQ-Orbitrap Velos mass spectrometer was utilized and its schematic is shown in Figure 8.[87] The instrument can be mainly divided into three parts: stacked ring ion guide, dual linear ion trap and combo C-trap/HCD collision cell, and they are applied to increase the ion flux, ion trap efficiency and detection speed, and fragment ion extraction respectively. Ion trap utilizes constant DC and radio frequency (RF) oscillating AC electric fields to trap ions and the stability region is related to the electric potential of RF and mass to charge ratio, as shown in equation below:[88]

$$s = \frac{4\mathrm{eV}}{\mathrm{m}r^2\Omega^2}$$

where V represents the electric potential of RF, e and m are the charge and mass of the ion respectively, $\Omega=2\pi\upsilon$ and υ is the applied frequency, r is a size parameter constant.

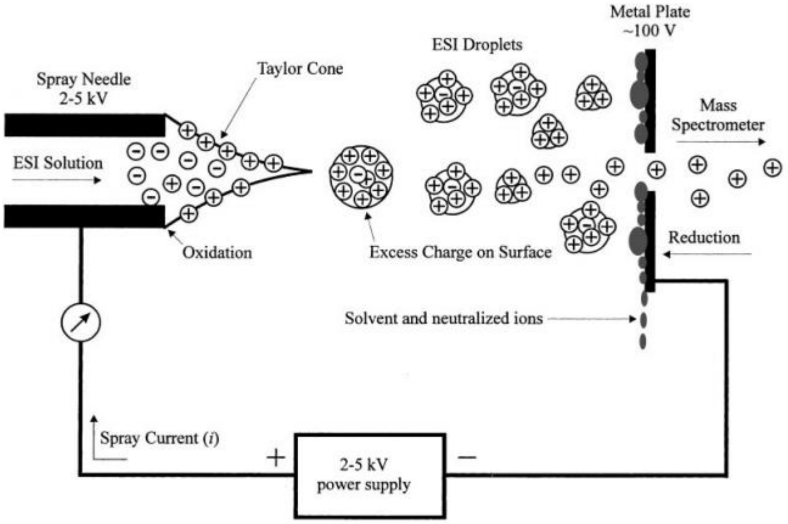

Figure 6. Schematic of electrospray ionization process, adopted from ref 84.

.

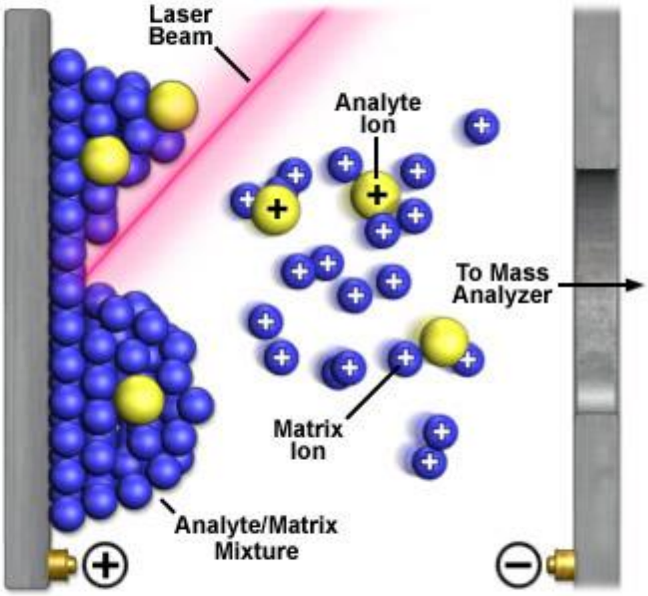

Figure 7. Schematic of matrix-assisted laser desorption ionization, adopted from ref 77.

Given the region is fixed, by increasing the electric, ions with specific mass to charge ratio will enter instability region and pull out in increasing order. Different from ion trop, which changes electric potential of RF to filter the ion, orbitrap can detect all ions simultaneously over a given period of time.[89] In orbitrap shown at the bottom in Figure 8, two electrodes-outer and inner-can form an electrostatic field with quadro-logarithmic potential distribution.[90] After injection of ions from C-trap into orbitrap, ions will move rotationally as well as back and forth along the axis of the central electrode. As a result, the orbital will look like helices, as demonstrated in the red line in Figure 8. Rotation movement is related to the initial velocity of the ions and when the ions reach the stability, the attraction between the ions and electrode will be balanced with the centrifugal force. As a result, different initial velocities will lead to different distances between the electrode and ions. Considering the axial motion, according to quadro-logarithmic potential distribution, the axial motion is harmonic,[91] meaning the frequency is only dependent on mass to charge ratio. So ions with same mass to charge ratio will move at the same frequency along the axis. After the injected ions reach the stable orbit inside the trap, ions with a specific mass to charge ratio will fall into rings which oscillate along the electrode and the axial oscillation of the ion rings are detected and transformed to final m/z data. Resolution can be improved by increasing the field strength and detection duration.

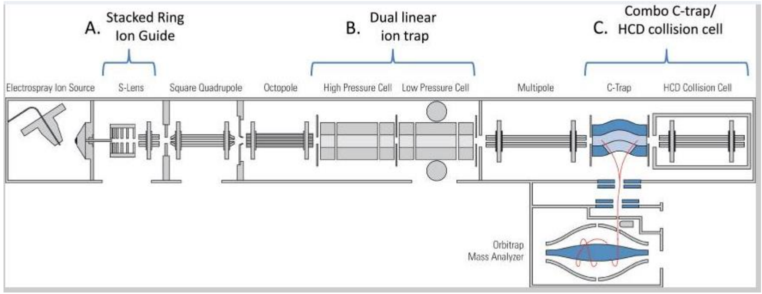

Figure 8. Schematic of Electrospray ionization mass spectrometry (ESI-MS) utilized, adopted from ref 87.

1.6.3. Nuclear Magnetic Resonance[92]

All isotopes with an odd number of protons and/or of neutrons have a nonzero spin, while all nuclides with an even number of both have a zero total spin. The nucleus has two possible spin states: m= ½ or m= - ½. When it is placed in a magnetic field, there is an interaction between the nuclear magnetic moment and the external magnetic field. As a result, the different nuclear spin states have different energies in a non-zero magnetic field, and this difference results in a small population bias between the two spin states. Only electromagnetic radiation of correct frequency which matches the energy difference between the nuclear spin levels in a constant magnetic field of the appropriate strength can be absorbed by nuclear spins. NMR spectroscopy is the techniques used to obtain physical, chemical, electronic and structural information from the resonant frequencies of the nuclei present in the sample. Proton (^{1}H) is the most commonly used spin ½ nucleus in NMR investigation. In the ^{1}H NMR spectrum, the chemical shifts and the spin-spin couplings are used to determine the chemical environment around the proton and then assign the molecule structure. Despite its relative abundance in nature (approximately 1%) in nature, ^{13}C is widely used and allows the identification of carbon atoms in an organic molecule. Heteronuclear Multiple-Quantum Correlation (HMQC is a 2D experiment used to correlate directly bonded carbon-proton nuclei which utilizes proton detection and has very high sensitivity. Heteronuclear Multiple-Bond Correlation (HMBC) is another 2D experiment (closely related to HMQC, its 1-bond analogue) used to identify long-range couplings between protons and carbons, generally referring to 2 or 3 bonds since couplings over more bonds are usually vanishingly small (exceptions include those across unsaturation).

2. RESEARCH PROGRESS

2.1. ESI-MS of Standard Compounds

As an accurate and precise instrument, ESI-MS is powerful in structure analysis, especially through tandem MS. However, since the soft fragmentation in ESI can be affected by various factors, no reliable standard spectra can be obtained from the database, like EI or other relatively hard ionization source. Standard analysis is required prior to unknown sample analysis. According to the literature, various oxygen containing functional groups can appear in the oxidation product of carbon nanomaterials[69] , as shown in Figure 9. Considering the oxygen containing functional groups, series of standards were chosen and analyzed in ESI to figure out the fragmentation pattern of aromatic hydrocarbons with –COOH, -OH and-CHO functional groups, including mellitic acid, 1,3,5-tricarboxylic benzene, benzoic acid, phenylacetic acid,

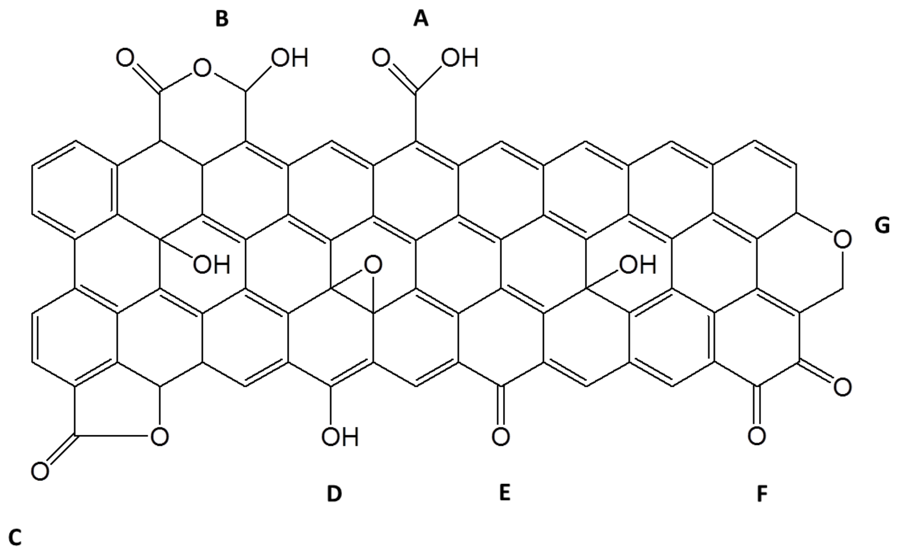

Figure 9. Oxygen containing functional groups
Different oxygen-containing functional groups on carbon nanomaterials, including Carboxyl groups (A), Carboxylic anhydride groups (B), Lactone groups (C), Phenol groups (D), Carbonyl groups (E), Quinone groups (F), Xanthene or ether groups (G).

benzaldehyde and 2,4-dihydroxybenzoic acid. The spectra show that in our system, -COOH tends to lose H_2O and CO or CO_2, -CHO tends to lose CO, -OH attached directly to the aromatic ring is stable and fragmentation tends to stop when conjugate structure is formed after the neutral molecules' loss. The pattern can provide practical information in the identification of the oxidation products.

2.2. General Rules for Tentative Structure Proposal

The first step in structure determination of the degradation products is element confirmation. It is reasonable to assume that all carbon atoms originate from the carbon nanomaterials, oxygen mostly from the oxidative reagent, and hydrogen from the carbon nanomaterials and solvent (H_2O). Nitrogen can be excluded based on the Nitrogen Rule (if odd number of nitrogen atoms is present, the m/z value will be an even number with +1 charge) and the specifics of the degradation experiment (no obvious nitrogen source). Another element that can be involved in the final product is chlorine, originated from hypochlorite reagent. However, it is excluded based on the isotope peak ratio of [M+2]/[M+1]. Since ^{37}Cl: ^{35}Cl=32.5%:100%, if Cl was present, the minimum ratio of [M+2]/[M+1] should be around 30%, which was not observed in our experiments. So only three elements, C, H and O were taken into consideration in structure proposal.

The second step in structure elucidation is to determine the chemical formula. The ESI-MS was utilized in the sample analysis; in most samples if not stated specifically, Orbitrap with 1 mDa resolution was used. The accurate and precise m/z value usually leads to only one possible formula consisting of different number of carbon, oxygen and hydrogen atoms. Charge of +1 is observed in most peaks based on value of isotope peak ([M+2]-[M+1]). From the formula, number of degree of unsaturation was calculated.

The third step is to figure out the possible functional groups and integration of information obtained to propose the structure. Since the fragmentation properties can be different in various ESI-MS instruments, a number of standards were analyzed prior to the actual degradation sample analysis to study the fragmentation pattern under specific conditions and certain patterns were learnt in –COOH, -CHO, -OH containing aromatic hydrocarbons.

However, some concerns should be kept in mind while elucidating the structures based mainly on MS data. First, even so only one possible formula can be deduced from MS data, the actual chemical structure can remain ambiguous. According to the Tandem MS, even if we could determine the type of functional groups, we would hardly know their relative position for sure, as a number of isomers would correspond to the same formula. Second, fragments with m/z lower than 1/3 that of parent ion cannot be detected in ion trap, as a result, some information might be lost. In addition, different mechanisms of fragmentation can make the system extremely complex and several factors should be taken into consideration, such as stability of fragment, rearrangement of unstable fragments, and electron distribution.

2.3. Photo Fenton Reaction of Graphene Oxide and Product Characterization

2.3.1. Experimental

Reagents and Materials. All the reagents were used as received without further purification. Graphene Oxide (GO) (5 mg/mL) was purchased from Graphene Supermarket in aqueous Solution. $FeCl_3$ (hexahydrate), 30% H_2O_2 and concentrated HCl were purchased from Sigma Aldrich. Solvents, including H_2O and MeOH were HPLC grade or higher.

Photo-Fenton Reaction of Graphene Oxide (GO). The photo-Fenton reaction was carried out under vigorous stirring in a 50 mL quartz tube, which was held around 6 cm from the UV lamp (Blak-Ray B100AP, 100-watt longwave UV, supplies fluorescence with ballasted bulb). In a typical experiment, 500 µL of 5 mg/mL GO aqueous solution, 4.5 µL of 30% H_2O_2, 100 µL of 1 mM $FeCl_3$ and 24.6 mL nanopure H_2O were mixed in the quartz tube. The pH of the mixture was adjusted to pH 4 with diluted HCl. The tube was sealed and 4.5 µL of 30% H_2O_2 was added on a daily basis to observe a complete degradation of GO during 3 days. After the reaction, the sample was filtrated through 0.2 µm filter paper. Partially oxidized GO was collected and its mass was measured on the filter paper after overnight drying in the oven.

Nuclear Magnetic Resonance (NMR). Samples after the reaction were filtrated through 0.2 µm filter paper. The filtrate was dried via lyophilization. The solid then was resuspended in D_2O to prepare an around 5mg/mL mixture. NMR spectra, including ^1H, ^{13}C, HMBC and HMQC were acquired using Bruker Avance III 400MHz and Bruker Avance III 500MHz.

UV-vis-NIR Spectroscopy. Aqueous samples (250 µL) were analyzed with a Lambda 900 spectrophotometer (Perkin-Elmer) in 500 µL quartz cuvettes (path length: 1cm, World Precision Instruments, Inc.) Samples with SWNTs were scanned from 200 to 1300 nm. Filtrates, which were expected to contain carboxylic aromatic hydrocarbon-like degradation products, were scanned from 200 to 400 nm.

Tandem MS Spectroscopy. Samples after the reaction were filtrated through 0.2 µm filter paper and the filtrate was dried via lyophilization (Labconco Freezone 6 Lyophilizer). Resuspension into ACN (acetonitrile):H_2O=1:1 with 0.1% formic acid (FA) or MeOH: H_2O=1:1 was performed by shaking with Vortex for 1 min to prepare solution around 1 mg/mL, which is subjected to a second filtration with 0.2 µm filter paper. LTQ Orbitrap-Velos MS instrument (Thermo Fisher Scientific) was used for mass spectra acquisition. Direct infusion experiment was performed with a nano ESI source. The voltage of the nano ESI tip was held at 1.75 kV and the entrance capillary was maintained at 200 ℃. Peaks in parent scan were selected, isolated and fragmented using collision induced dissociation (CID) to obtain MS/MS spectra. Both positive mode and negative mode were performed.

High-Performance Liquid Chromatography (HPLC). Samples after the reaction were filtrated through 0.2 µm filter paper. An hp (Hewlett-Packard) series 1100 HPLC system equipped with both a photodiode array detector was applied for separation. Separation was carried out at 0.2 mL/min flow rate at 250 nm. The chromatographic column was an Agilent PL-SAX 1000Å (2.1 mm i.d. ×150 mm length). Gradient elution was conducted as reported, in which concentration of ammonium acetate (pH 7.0) was increased from 240 mM to 600 mM over 14 min and then was held at 600 mM for 30 min.

AFM. Veeco Dimention^{TM} 3100 atomic force microscope was utilized in a tapping mode for height, phase, and sectional analysis. Sample preparation was performed on freshly washed Si wafer treated with piranha solution (7:3 concentrated H_2SO_4: 35% H_2O_2, 70℃). Approximately

10 μL of the sample (aq) was spin-coated at 1400 rpm to get an even and smooth distribution of the sample on the wafer surface.

Raman. Samples were prepared by spin-coating approximately 10 μL of graphene oxide solution at day 0, day 1 and day 3 at 1400 rpm on fresh prepared silica wafers (piranha solution, 7:3 concentrated H_2SO_4: 35% H_2O_2, 70℃). All spectra were obtained on Renishaw *inVia*Raman microscope at an excitation wavelength of 633 nm. Multiple scans from 1000 to 3000 cm^{-1} were applied and averaged to determine the D and G bands.

2.3.2. Results and Discussion

- **Characterization of Graphene Oxide in Solution**

The unique character of Photo Fenton Reaction makes it a perfect system for identification of oxidation products of carbon nanomaterials. Compared with NaClO and MPO degradation system for carbon nanomaterials, Fenton Reaction is relatively simple, with low concentration of Fe^{3+}/Fe^{2+} and H_2O_2, which can be removed via freeze-drying. This character makes it MS-friendly, in terms of salt concentration. In addition, introduction of high power UV lamp can control the reaction rate effectively. In this part, Photo Fenton Reaction was applied to degrade GO completely within 3 days, and Raman, AFM and UV were used to monitor the reaction process. As evidence of degradation during 3 days, Figure 10B shows photographs of initial vial with GO (left) versus day 1 (middle) and day 3 (right) incubation with $FeCl_3$ and H_2O_2 under UV irradiation. The color changed from brown to dark, indicating the size reduction of GO, and then turned to almost clear, confirming the complete degradation of GO. In Figure 10C, both D and G bands were present at day 0 and day 1, indicating the sp^2 hybridized carbon and graphitic carbon structures. For day 3, neither D nor G was observed, confirming the degradation of graphene oxide. Figure 10D shows AFM tracking of as-received GO and GO degraded by $FeCl_3$ and H_2O_2 over 1 day and 3 days. As can be observed, prior to incubation, dimension of the graphene oxide flakes were approximately 600 nm with a broad distribution. After 1 day, the size reduced significantly to around 358 nm with a narrow distribution and the height remained similar to day 0. After 3 days reaction, small particles with 2 to 5 nm height were present, indicating the oxidation of GO and the formation of Graphene Quantum dots (GQDs). In addition, the degradation process was studied spectroscopically. UV-Vis absorption spectroscopy measurements were taken on day 0, day 1 and day 3 of GO after photo Fenton reaction (Figure

10E). For GO (bottom red), absorption peak around 220 to 250 nm was observed confirming the characteristics of as-received GO. After 1 day and 2 days incubation, the peak disappeared as a result of degradation. For day 3 sample, broaden peak from 200 nm to 250 nm indicated the existence of newly produced substance with conjugated system. Figure 10E depicts the UV spectra of standard compounds-1,3,5-tryoxybenzoic acid and benzoic acid. 1,3,5-tryoxybenzoic has an increasing absorption from 220 nm to 200 nm and benzoic acid has a peak at 130 nm. Those peaks can be explained by conjugated system and effect of carboxylic functional group. In our research, a broad peak from 200 nm to 260 nm was observed (Figure 10 D, blue), which is consistent with the peaks shown in standard compounds with conjugated system and C=O double bond. In addition, the broadness of the peak can result from the overlapping of peaks from the mixture of the degradation products. In other words, even if the individual products have unique adsorption peaks, the overall peak can be broadened because of the contribution of various adsorption peaks.

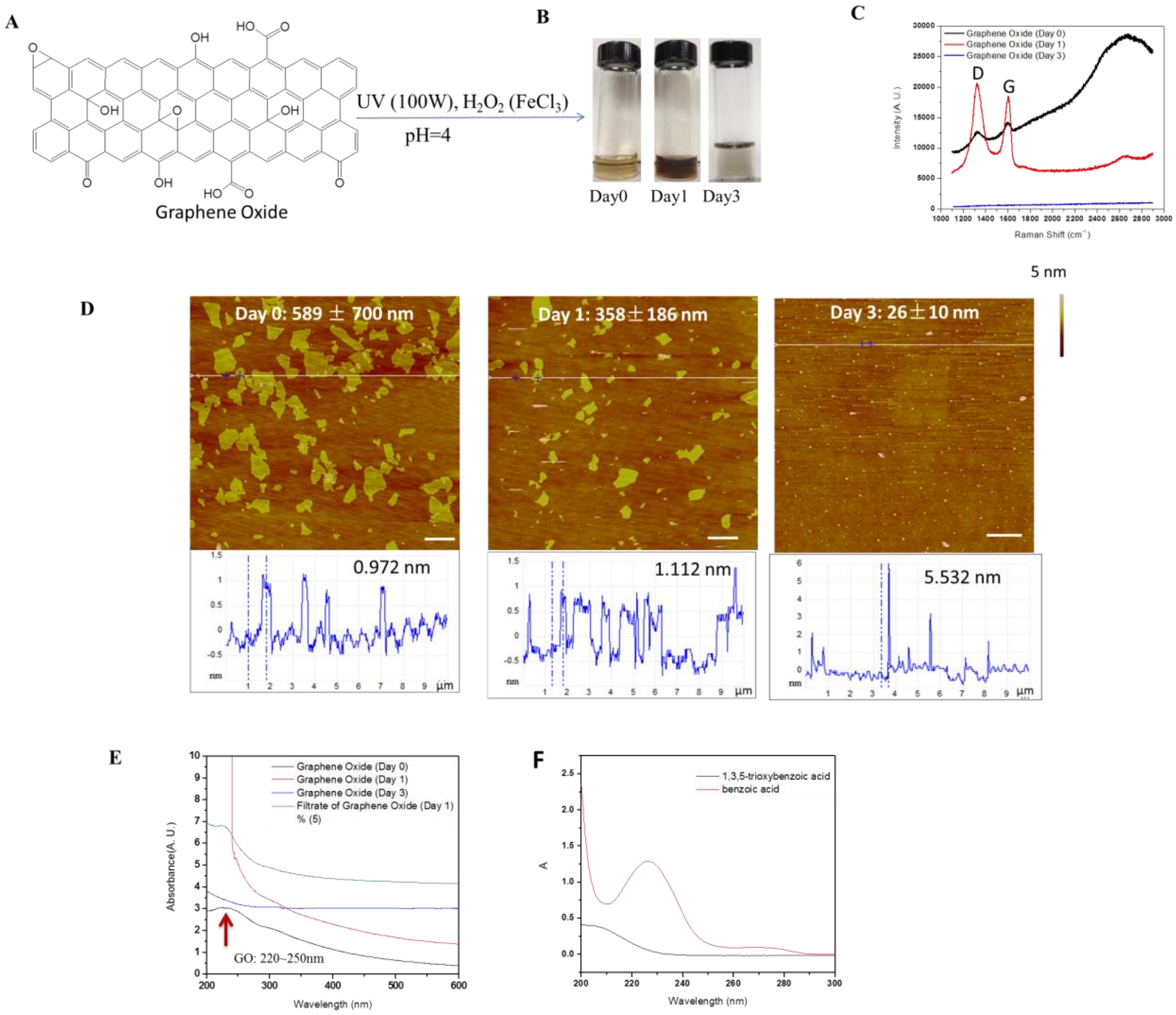

Figure 10. Characterization of Graphene Oxide

(A) Scheme of Graphene Oxide with various oxygen-containing functional groups. (B) Photograph demonstrating the degradation of GO with Photo Fenton Reaction during the 3 days of the reaction. (C) Raman spectra of photo Fenton reaction of GO at day 0 (black), day 1(red) and day 2 (blue). The D and G bands are marked on the spectrum. (D) AFM image of as-received GO (left) and after photo reaction of 1 day (center) and 2 days (right). Section analysis was applied at positions marked with blue “plus sign”. All images were obtained using tapping mode. Scale bars are 1 µm. Length distributions of Day 0 and Day 1 samples are as marked in white numbers. (E) UV spectra confirming the degradation of GO and formation of oxidation products. (F) UV spectra of two aromatic acids: 1,3,5-trioxybenzoic (black) acid and benzoic acid (red).

The reaction rate can be controlled and optimized by changing the UV power absorbed in unit vial surface, which can be affected by various factors. The most effective one is the change of UV lamp power, while it was not practical in our lab. Another factor is the size of the vial. Two vials of 5 mL and 50 mL were utilized, demonstrating significant different reaction rate. In 50 mL vial, it took 3 days to completely degrade GO with $FeCl_3$ and H_2O_2, while to obtain the same result, it took only 1 day in 5 mL vial. Another factor is the distance between the UV lamp and the quartz vial. For reaction in 5 mL vial, two distances of 6 cm and 10 cm were tested. It took more than two days for the 10 cm GO sample to be degraded completely. One explanation is that at the longer distance, the photon number in unit surface will decrease, meaning that the irradiation intensity in unit surface will decrease with the increase in distance. According to the equation, $Fe^{3+} + H_2O_2 + hv \rightarrow Fe^{2+} + OH^{\bullet} + H^{+}$, giving that hv is higher than the activation energy of the reaction, the production of $OH^{\bullet}$ radicals will be accelerated with more photon introduction. Another explanation for the increased reaction rate with shorter distance would be the heat adsorption from the UV lamp, for a specific range, leading to an increase in reaction rate constant.

To sum up, Photo-Fenton Reaction is effective in increasing the reaction rate, although the exact extent of the increase still remains unknown and no research on systematical study of kinetics of the reaction was performed so far. In my research, the focus is on the elucidation of products, and the main target is to produce plenty of products within a relatively short time reproducibly.

- **Functional Groups Determination and Identification of Small Oxidation Products**

In Photo-Fenton Reaction, the system is simple. H_2O_2 can be removed by freeze-drying of the solvent and the only interference source of ion is Fe^{3+}/ Fe^{2+}, which is at negligibly low concentration (4×10^{-6} M). The only treatment prior the MS injection is removal of solvent by freeze-drying after filtration through 0.2 μm filter paper to concentrate the degradation products. The adoption of freeze-drying cannot only remove the solvent without introduction of potential contamination, but also remove the remaining H_2O_2 without further oxidation. Figure 11 depicts the parent scan MS spectrum. Tremendous high intensity peaks were present only in the sample,

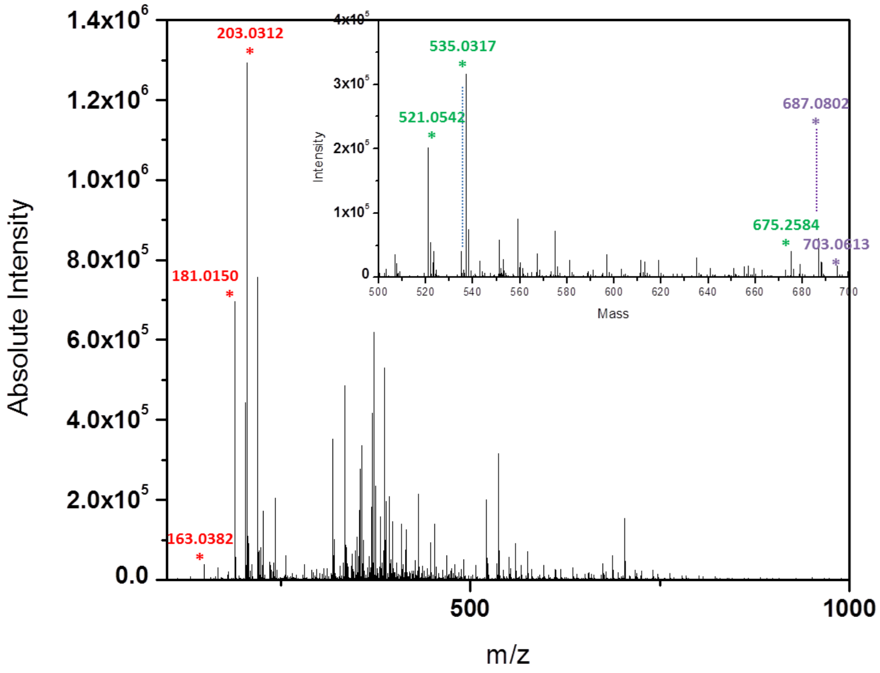

Figure 11. Mass spectrum of GO degradation products
Parent MS spectrum demonstrates the GO degradation product with $FeCl_3$ and H_2O_2 incubation for 1 day.
Inset shows magnification of peaks with m/z from 500 to 700 nm.

* MS was done by Wentao Jiang (Robinson Research Group)

indicating the existence of the intermediate substance whose signal was not suppressed by the salt. Some of the peaks with small m/z values were identified with plausible structure after analysis, as labeled with red asterisk. In the high m/z value region, though no reliable structures were proposed because of the complexity of fragmentation, certain interesting fragmentation patterns were observed.

In the small m/z value region, given the accurate and precise parent scan MS and Tandem MS, formulas and potential functional groups can be determined and tentative structures can be proposed with relatively high certainty. Furthermore, peaks in parent scan are not all independent from each other. First, one peak might be fragment or precursor of another peak. In analysis of standards, fragmentation, especially the loss of neutral molecules such as H_2O, can occur even in the parent scan. Second, the molecules may share certain structure and differ from each other at certain stable functional groups. In this case, the Tandem mass spectrum of the molecules can have the similar fragmentation pattern, in terms of sequence of mass loss.

We successfully proposed several structures. For example, in the representative peak from 189 and 203, both of which are among the most intense peaks in parent scan, similar fragmentation pattern was observed as shown in Figure 12. In both of the MS/MS spectra, m/z=171.0042 was dominant, indicating that m/z=189 and m/z=203 share the same stable fragment, m/z=171, which is stable because of the conjugated π bond. Following the general rules, according to the parent scan, formulas were first determined as $C_{10}H_4O_4$ and $C_{11}H_6O_4$, with Δm equals to 17.4 ppm and 15.9 ppm respectively. For both peaks, degree of unsaturation is 9, which is high considering such a small molecular weight, suggesting the possibility of aromatic structure and C=O double bonds. Based on the information from parent scan, considering the high degree of unsaturation of relatively small molecule, limited number of structure frames can be constructed in the form of adjacent aromatic rings or quinone-like structure. From the Tandem MS spectrum at m/z=189, H_2O loss is predominant and indicated the appearance of active –OH or –COOH, while –COOH can be excluded for the lack of CO_2 loss. After applying those rules, only one plausible structure was proposed (Figure 12C). For Tandem MS at m/z=203, the H_2O loss was replaced by CH_4O loss, indicating that $–CH_3O$ shares the same position as –OH in m/z=189, as shown in Figure 12C. The proposed structure is consistent with the information in MS and supported by NMR data (see the following discussion) and the stability of the structure is satisfactory with oxygen containing functional groups we expected. Another set of plausible structure was proposed following the similar analysis procedure, shown in Figure 13. To sum up, the method is effective, especially for the small molecules.

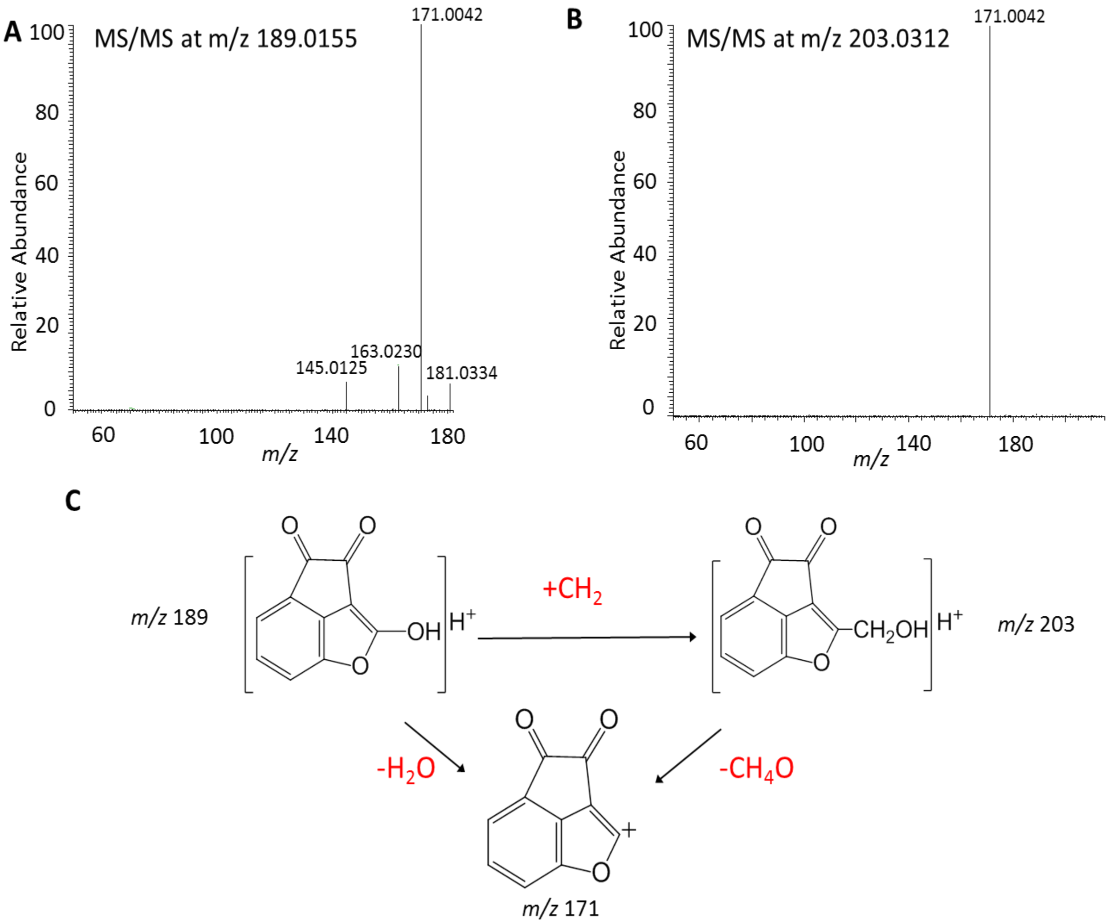

Figure 13. Tandem MS
(A) Tandem MS at m/z=189.0155. (B) Tandem MS at m/z=203.0312. (C) Fragmentation mechanism at the two m/z values and corresponding structures.

*MS was done by Wentao Jiang. (Robinson Research Group)

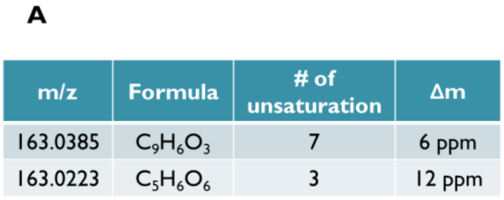

m/z	Formula	# of unsaturation	Δm
163.0385	$C_9H_6O_3$	7	6 ppm
163.0223	$C_5H_6O_6$	3	12 ppm

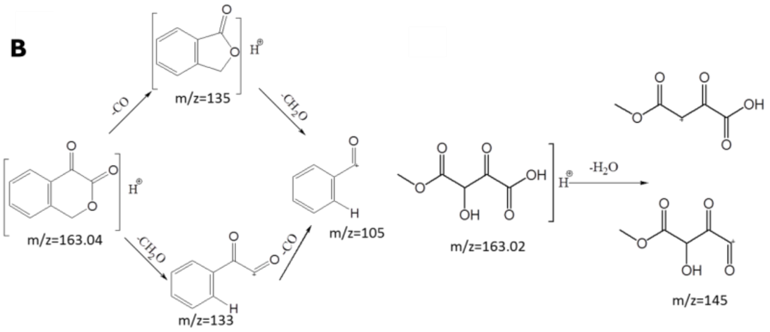

Figure 12. Proposed structures
(A) Formula and degree of unsaturation of two peaks from parent scan. (B) Proposed structures and fragmentation mechanism in Tandem MS.

To confirm the type of functional groups shown in the degradation products, ^{1}H-NMR, ^{13}C-NMR and three types of 2D NMR, including correlation spectroscopy (COSY), heteronuclear multiple quantum coherence-direct C-H coupling (HMQC) and heteronuclear multiple bond coherence-2-4 bond coupling (HMBC), were performed.

Figure 14A demonstrates the ^{1}H NMR. Chemical shift at 4.62 ppm can be assigned to the solvent D_2O. The region in the range 7 – 8 ppm is characteristic of aromatics. The signals due to α-substituent groups (CH/CH_2) of the aromatics appear in the region 2.5–2.8 ppm. For the region from 0.5 to 1.5, a broad assignment in terms of CH*n* (*n*=1,2,3) groups is possible. Because the active proton from the product can exchange with proton in the solvent D_2O, no signal from active proton, such as –COOH and –OH, was collected.

In Figure 14B, the COSY spectrum depicts the proton coupling through limited number of chemical bonds (usually less than 4). The peaks can be divided into two groups: diagonal peaks sharing the same frequency coordinate as each axis and off-diagonal or cross peaks indicating the couplings between pairs of proton, and the latter is what we want to focus on. The peaks in the blue arrow pointed region can be assigned to the multiple aromatic protons. The spot with red arrow can be assigned to coupling between aromatic proton and -CH*n* (*n*=1,2,3) and the spot with green arrow indicates the coupling between Ar-CH and -CH*n* (*n*=1,2,3).

In Figure 14C, ^{13}C spectrum indicates characteristic of aromatics and heteroaromatics (128 - 132 ppm) and that of carboxylic acid and esters (172 ppm). Although not enough information about the functional groups obtained from proton NMR resulting from the proton exchange mentioned above, the ^{13}C spectrum supports the presence of oxygen containing functional groups.

In HMQC (Figure 14D), which represents the direct C-H coupling, adjacent relationship between hydrogen and carbon was reflected. Besides aromatic hydrogens, various oxygen-containing functional groups, as we expected, can appear in the oxidation products. Although the degree of unsaturation is high, concluded from the MS data, there are still saturated alkanes. In addition to the direct coupling, HMBC (Figure 14E), indicating the coherence of 2-4 bond coupling, provided strong evidence of quinone functional group, which we applied frequently in elucidation of the structures.

To sum, NMR spectra support the presence of aromatic protons and various kinds of oxygen containing functional groups, which is of great help in elucidation of potential structures of the oxidation products.

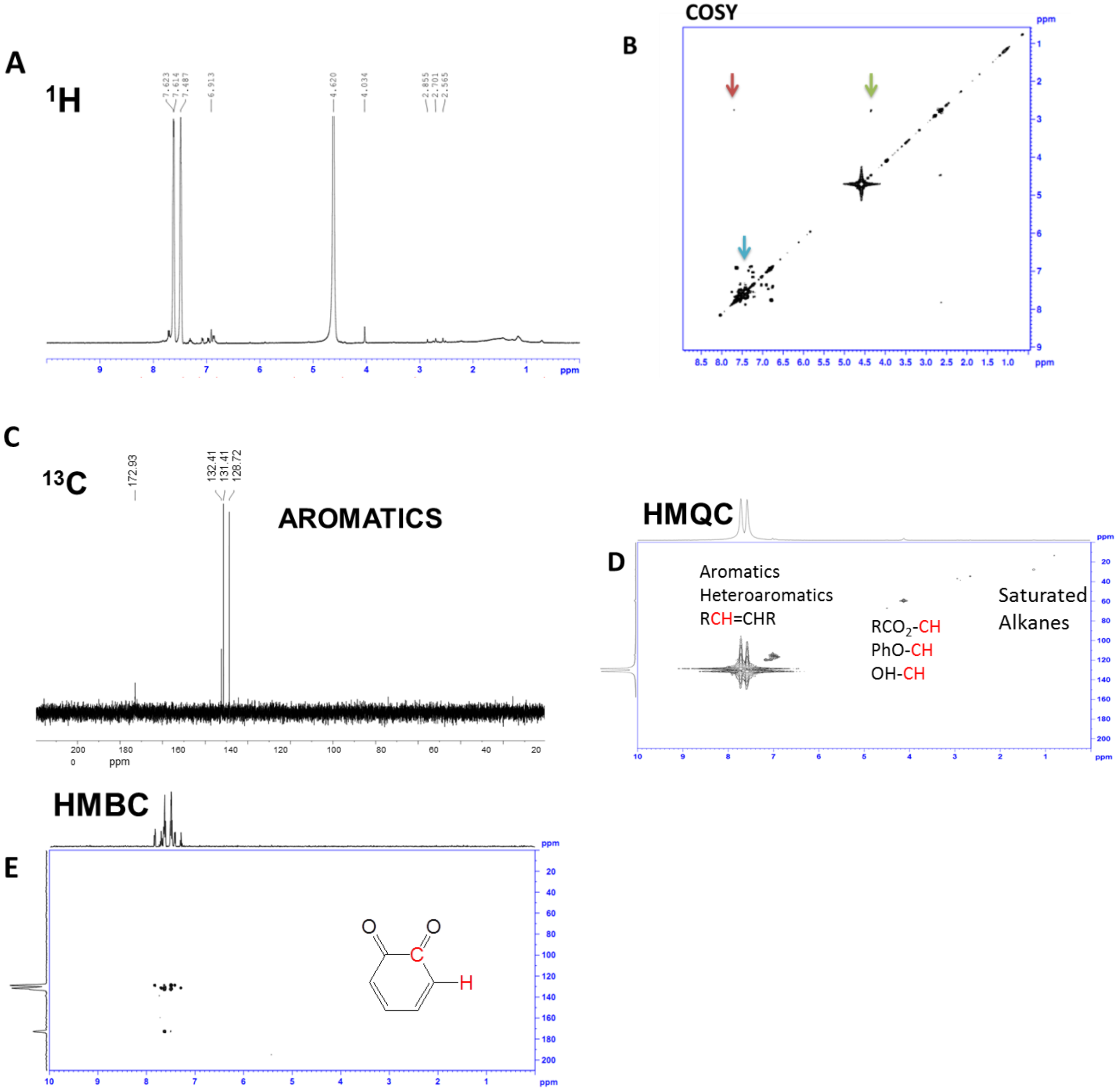

Figure 14. NMR spectra

NMR spectrum indicating functional groups presented in oxidation products from Photo Fenton reaction of GO, ^{1}H (A), Correlation spectroscopy (COSY) (B) ^{13}C (C), Heteronuclear Multiple Quantum Coherence of direct C-H coupling (HMQC) (D) and Heteronuclear Multiple Bond Coherence of 2-4 bond coupling (HMBC) (E).

- **Monitoring the Morphology Transformation of GO by AFM**

To study how individual GO flakes change over time during the Photo Fenton Reaction, AFM was used to image the same location and demonstrate the morphology transformation, as shown in Figure 15. At the early stage in Figure 15, a significant increase in average height was observed and several dots of height around 10 nm-20 nm appeared. To explain the height increase, contamination introduction or salt residue was excluded from the controls. One plausible explanation is that at the early stage reaction, reaction products attached to the GO sheets surface and formed an additional layer. As for the big dots, since they only appeared at the early stage, we assume they were products from the reaction. With time increasing, at the

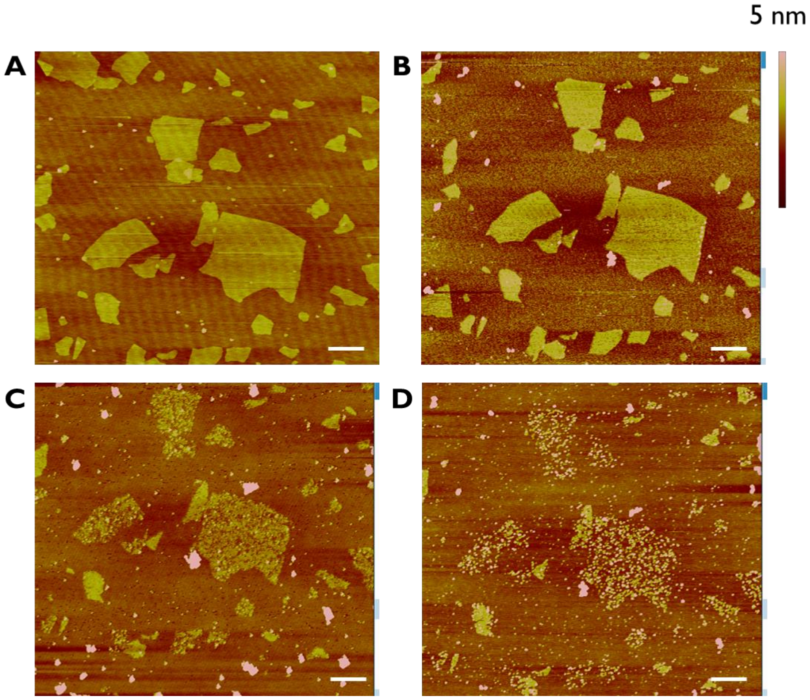

Figure 15. On-chip AFM images of Graphene Oxide Oxidation
AFM images of as-received GO (A), and after reaction with the Fenton reagent under a UV irradiation for 18 hr (B), 36 hr (C) and 54 hr (D), respectively. All images were obtained using tapping mode. Scale bars are 500 nm.

middle stage (Figure 15C), some holes were observed on the basal plane of the GO sheets and the overall height decreased. After 54 hr of the reaction, most of the GO flakes were cut into Graphene Quantum Dots (GQDs).

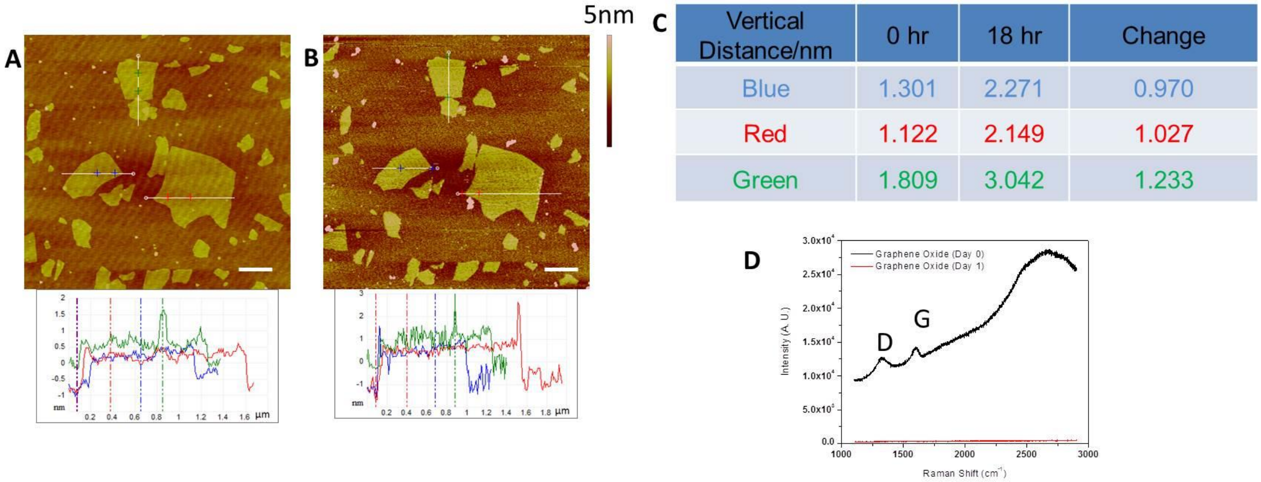

Vertical Distance/nm	0 hr	18 hr	Change
Blue	1.301	2.271	0.970
Red	1.122	2.149	1.027
Green	1.809	3.042	1.233

Figure 16. Height profile of GO Oxidation at early stage
AFM image of as-received GO (A) and after reaction of Photo Fenton Reaction for 18 hr(B). Section analysis was applied at positions marked with blue, red and green “plus sign” to indicate the height change. All images were obtained using tapping mode. Scale bars are 500 nm.C. Summary of the height of GO sheets before and after the Photo Fenton Reaction, and the corresponding change in those three positions. D. Raman spectra of as-received graphene oxide (black) and after 18 hr reaction with $FeCl_3/H_2O_2$ under UV irradiation (red). The D and G bands are marked on the spectrum.

Section analysis on as-received GO and after 18 hr reaction GO was done to demonstrate quantitatively the height change at the early stage, as shown in Figure 16. Three representative positions, marked in blue, red and green, were analyzed. Blue and red are single layer GO (height ~ 1 nm) and green is double layer GO (height ~ 2 nm). In both Figure 16A and Figure 16B, the surface of the GO was relatively flat, which indicated that either the height increase did not have much selection or the reaction products could be relatively evenly distributed on the surface of the GO. From Figure 16C, the height increase during the early stage was around 1 nm. This observation was consistent with our mass spectrum, which indicated the production of relatively small molecules. In addition, Raman spectroscopy was utilized to analyze the on-chip graphene oxide and GO after 18 hr reaction of photo Fenton reaction, in which both D and G bands disappeared. This change might be caused by the coverage of the additional layer.

At the middle stage, holes appeared on the GO sheets (Figure 17A) and the overall height decreased (~1 nm) compared with early stage (~ 2 nm) (Figure 17C). After 54 hr, the preserved motif was cut into GQDs with an average lateral size of 50 nm and the thickness of 3 nm.

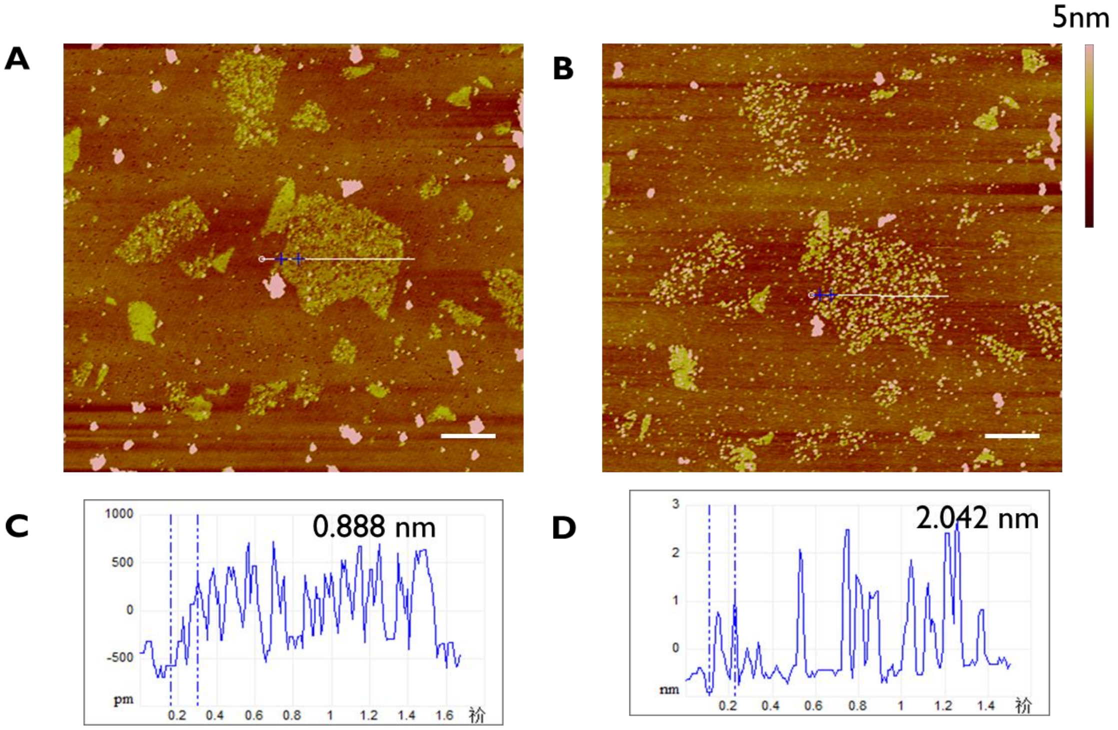

Figure 17. Section Analysis GO Oxidation

Section analysis of 36 hr (A) and 54 hr (B) after photo reaction of GO. Section analysis was applied at positions marked with blue “plus sign”. All images were obtained using tapping mode. Scale bars are 500 nm.

As control experiments, we conducted the photo reaction of GO in water without photo reagent (control I, Figure 18) and Fenton reaction of GO without UV (control II, Figure 19). In control I (Figure 18), no significant increase in height was observed and no holes were formed on basal planes after 2 days reaction. Meanwhile, in control II, in which Fenton reaction of GO was conducted under a dark condition for 36 hr, no height increase/holes were observed either. These results confirmed that both UV and Fenton reagent are necessary for the rapid degradation of GO into GQDs.

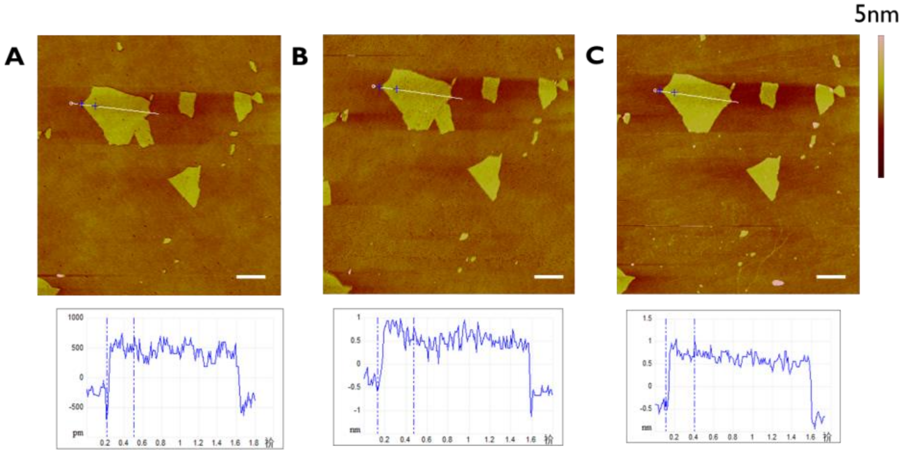

1.241 nm 1.394 nm 1.295 nm

Figure 18. AFM images of control experiment (I)

Section analysis of as-received GO (A), after photoreaction under a UV irradiation without the Fenton reagent for 1 day (B) and 2 days respectively. The height profile is from the white line and the vertical distance was measured from two blue "plus sign" as marked. All images were obtained using tapping mode. Scale bars are 500 nm.

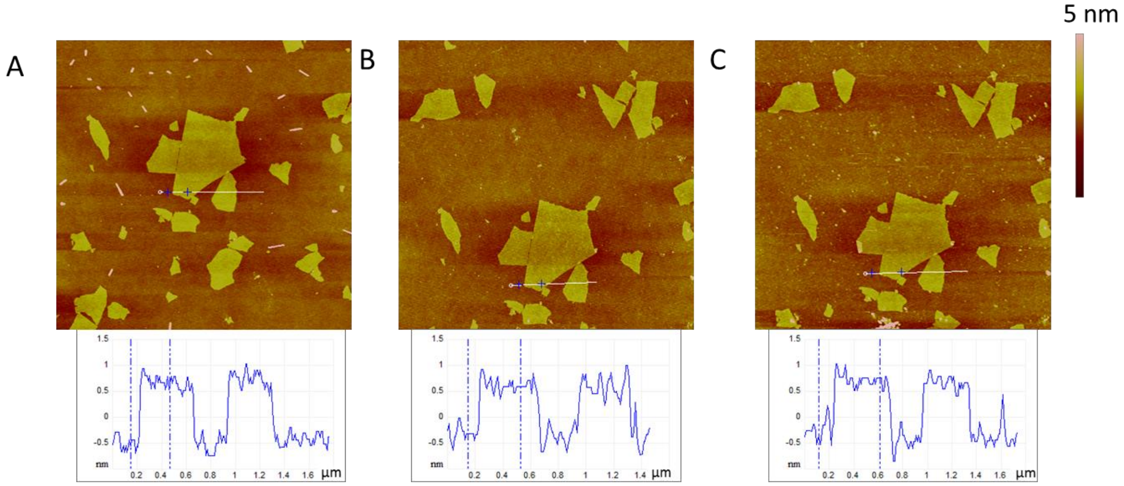

1.217 nm 1.105 nm 1.156 nm

Figure 19. AFM images of control experiment (II)

Section analysis of as-received GO (A) and after reaction with the Fenton reagent without UV for 18 hr (B) and 36 hr (C). The height profile is from the white line and the vertical distance was measured from two blue "plus sign" as marked. All images were obtained using tapping mode. Scale bars are 500 nm.

2.4. Identification of Degradation Products in MPO and NaClO system

2.4.1. Experimental

Reagents and Materials. Single-walled carbon nanotubes (SWNTs) were purchased from Carbon Solutions, Inc. (P3-SWNT samples), which were prepared by arc-discharge process[23], followed by nitric acid treatment, leaving them in highly functionalized form, containing 1.0 – 3.0 atomic% carboxylic acid. Myeloperoxidase (MPO), from human neutrophils, was purchased from Athens Research & Technology. NaClO, $FeCl_3$ (hexahydrate), 30% H_2O_2 were purchased from Sigma Aldrich. Amplex Red was procured from Molecular Probes, Invitrogen. Solvents, including H_2O, MeOH, MEK, ACN, Ethyl Acetate, dichloroform and etc. were HPLC grade or higher.

Incubation of P3-SWNTs with MPO and H_2O_2. 100 μg MPO was suspended in 360 μL pH 7.4 PBS buffer. In a typical experiment, 4 μL of MPO solution prepared as described above, producing a minimal activity of 800 μU/μL, 15 μL of 1mg/mL SWNTs, 1 μL of 18.75mM H_2O_2, 7 μL of 5M NaCl and 180 μL PBS buffer were mixed thoroughly to start the reaction in the incubator at 37 ℃, followed by hourly addition of 1 μL of 18.75mM H_2O_2 eight times per day and daily addition of 4 μL of MPO stock solution. This reaction can be scaled up if necessary. The reaction continued for 4 days. All the stock solutions were kept in the refrigerator at 4 ℃. Activity of MPO was tested and verified with Amplex Red before the reaction.

Incubation of P3-SWNTs with hypochlorite. SWNTs was suspended with sodium hypochlorite (10~15% available Cl) to make a 1mg/mL SWNTs solution. The reaction was conducted at different temperatures from room temperature to 80 ℃ under vigorous stirring with reflux. The reaction continued for 24 hrs before further characterization.

UV-vis-NIR Spectroscopy. Aqueous samples (250 µL) were analyzed with a Lambda 900 spectrophotometer (Perkin-Elmer) in 500 µL quartz cuvettes (path length; 1m, World Precision Instruments, Inc.) Samples with SWNTs were scanned from 200 to 1300 nm. Filtrates, which were expected to contain carboxylic aromatic hydrocarbon-liked degradation products, were scanned from 200 to 400 nm.

Tandem MS Spectroscopy. Samples after the reaction were filtrated through 0.2 µm filter paper. Unreacted SWNTs were collected on the filter paper after drying in the oven overnight. Filtrates were first acidified with HCl, and then collected for further deionization treatment. Purification treatments including extraction with organic solvents, solid phase extraction (SPE) column and dialysis were performed as mentioned below. After the purification, solvent was removed by rotary evaporator or speed vac. Resuspension into ACN (acetonitrile):H_2O=1:1 with 0.1% formic acid (FA) or MeOH: H_2O=1:1 was performed by shaking with Vortex for 1 min to prepare solution around 1 mg/mL, which is subjected to a second filtration with 0.2 µm filter paper. LTQ Orbitrap-Velos MS instrument (Thermo Fisher Scientific) was used for mass spectra acquisition. Direct infusion experiment was performed with a nano ESI source. The voltage of the nano ESI tip was held at 1.75 kV and the entrance capillary was maintained at 200 ℃. Peaks in parent scan were selected, isolated and fragmented using collision induced dissociation (CID) to obtain MS/MS spectra. Both positive mode and negative mode were performed.

Extraction with Organic Solvent. Extraction with methyl ethyl ketone (MEK), ethyl acetate and dichloromethane was conducted. Typically, equal volumes of organic solvent and aqueous solution were mixed and shaked vigorously. Extraction was usually performed three times and organic phase was collected for rotary evaporation.**Solid Phase Extraction (SPE).** SPE was performed with Oasis Cartridge column (10 mg) under controlled vacuum. The column was first washed with H_2O (50%)/ACN (50%) with 0.1% FA. Then ACN, with 0.1% FA, was injected to degas the column and H_2O, with 0.1% FA to equilibrium the column. Sample was injected (approximately 1mg in total mass) and 2-3mL H_2O was applied to wash away the salt. Finally, 1 mL of H_2O (50%)/ACN (50%) with 0.1% FA and 250 μL of ACN, with 0.1% FA, was injected accordingly to elute the substance attached to the column stationary phase.

C18 Ziptip. C18 Ziptip(Supelco, Bellefonte, PA) was equilibrated with 10 μL ACN (with 0.1% FA) twice followed by 10 μL H_2O (0.1% FA). Sample was aspirated into the Ziptip and dispensed for 3-5 times to allow product binding to the column packing material. Column was washed twice with H_2O (0.1% FA) for desalination and binding compounds were eluted with ACN (0.1% FA) into an Eppendorf tube.

Dialysis. Dialysis was performed utilizing tube with molecular weight cutoff of 500 Da (Sigma). The reaction products were dialyzed in nanopure water for 2 days to remove the small molecules, ideally, only salts and H_2O_2. Small molecular weight cutoff tubes were applied to reduce the loss of the oxidation products. The dialysis time was controlled to balance the desalination and loss of the oxidation products.

High-Performance Liquid Chromatography (HPLC). Samples after the reaction were filtrated through 0.2 μm filter paper. A Waters 600 analytical HPLC system equipped with both a 996 photodiode array detector and 2410 refractive index detector was applied for separation. For Reversed Phase Liquid Chromatography (RPLC), the filtrate was acidified with HCl, and either a Waters Nova C18 was utilized. For Ionic Exchange Chromatography (IEC), Agilent Zorbax

Strong Anionic Exchange (SAX) was utilized, and the filtrate was injected to the column directly. Various different programs were studied to optimize the separation.

Liquid Chromatography Mass Spectrometry. After reaction, the samples for LCMS were treated in a similar way as those were treated in MS. After filtration through 0.2 μm filter paper, filtrates were acidified with HCl and purified with various methods, including extraction with organic solvents, SPE column and dialysis. Solvent was removed afterwards by rotary evaporator or speed vac. The solid was resuspended into ACN: H_2O=1:1 with 0.1% FA or MeOH: H_2O=1:1 via shaking with Vortex for 1 min and the final concentration was around 1 mg/ mL. A second filtration through 0.2 μm filter paper was performed prior to the injection into LCMS. Approximately an aliquot of 1-5 μL concentrated sample was injected to LCMS-2020, Shimadzu Instrument, equipped with Shimadzu Ultra Fast Liquid Chromatography inlet system, coupled with electrospray ionization (ESI, ±ve), and atmospheric pressure chemical ionization (APCI, ±ve). Typically a 35-min gradient program was performed: the column was eluted with gradient solvent from A:B (10:90) to A:B (0:100) at a flow rate of 0.30 mL/min , where A is aqueous formic acid (0.1% (v/v) formic acid) and B is acetonitrile (0.1% (v/v) formic acid). The full scan data was acquired from *m*/*z* 50–2000 with a 0.3 s scan time, using a capillary voltage of 3.0 kV for the positive ion mode or negative mode.

AFM. Veeco Dimention^{TM} 3100 atomic force microscope was utilized in a tapping mode for height, phase, and sectional analysis. Sample preparation was performed on freshly washed Si wafer treated with piranha solution (7:3 concentrated H_2SO_4: 35% H_2O_2, 70℃). Approximately 10 μL of the sample (aq) was spin-coated at 1400 rpm to get an even and smooth distribution of the sample on the wafer surface.

2.4.2. Results and Discussion

2.4.2.1. Chemical Degradation of SWNTs with NaClO at High Temperature

- **Characterization of SWNTs**

To confirm and monitor the degradation process, nanomaterial characterization using TEM and Raman was performed. Figure 20 depicts photograph and TEM images of the degradation reaction. In Figure 20A, photographs of the first 3 hr reaction are demonstrated. When the reaction started, the color of SWNT suspension was dark brown. With the relatively fast degradation reaction, visible color change could be observed during the first 1 hr, turning to light brown or yellow, and afterwards, the color remained similar till 24 hr reaction was finished. The color was determined by the color of NaClO, which is yellow, and that of small amount of unreacted P3-SWNTs. TEM images (Figure 20B-D) reveal the SWNT degradation. In the first 4 hr, the length of P3-SWNTs decreased significantly from 487 nm for one hour reaction to 374 nm for 2 hour reaction (Figure 20C-D). After 1day, it was hard to observe the linear structure of P3-SWNTs, which meant the degradation, to large extent, was completed. Figure 21 shows the Raman spectra of SWNTs during the first day oxidation. Both D and G band decreased significantly during the reaction, by comparison between 1hr and 1Day sample. From Figure 21B, the D/G ratio increased at first, indicating the production of defects on the SWNTs, and then decreased, which can be explained by SWNTs breaking apart from the defects.

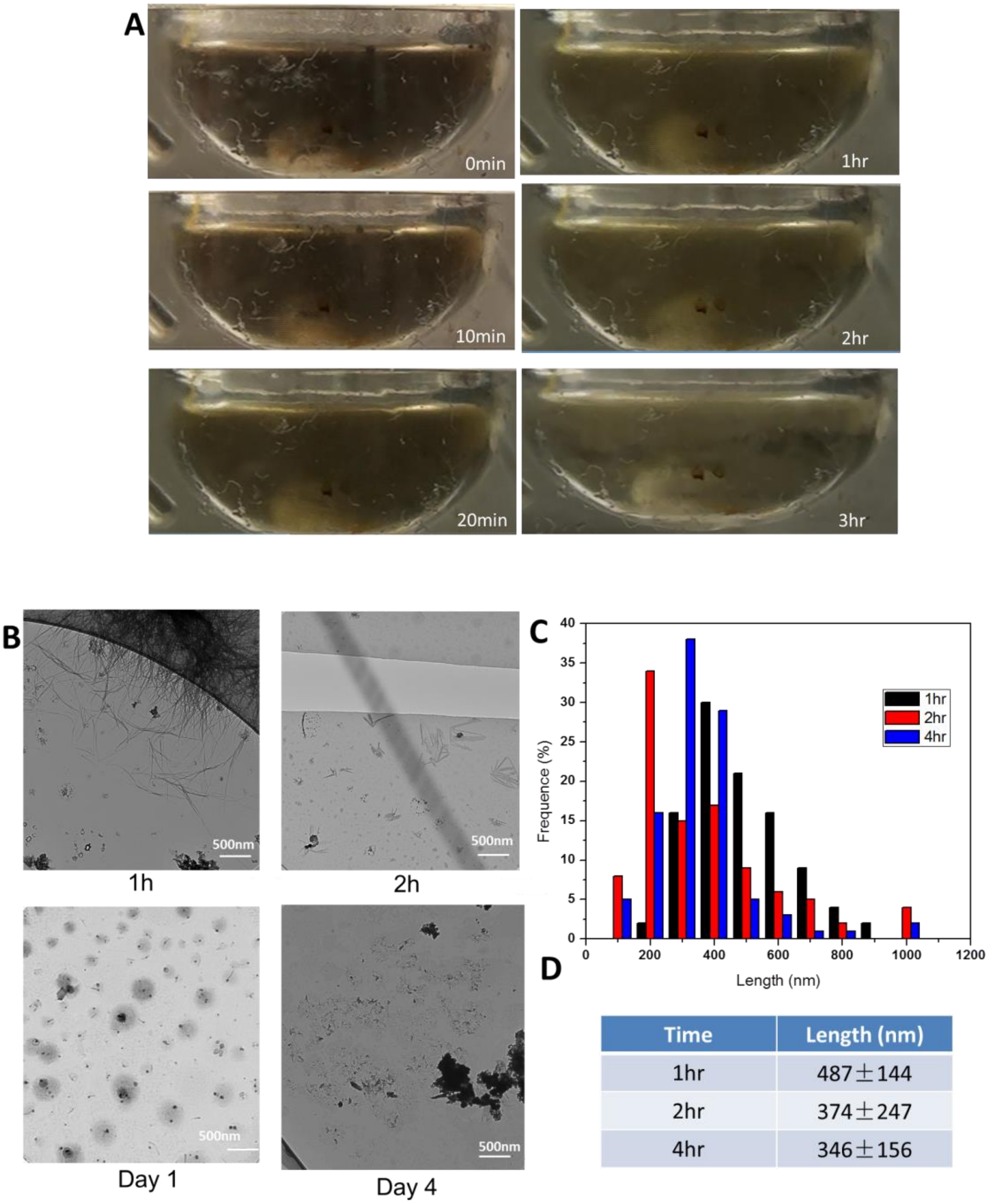

Time	Length (nm)
1hr	487±144
2hr	374±247
4hr	346±156

Figure 20. Characterization of SWNTs

(A) Photograph demonstrating the degradation of P3-SWNTs with NaClO during the first 3hr of the reaction. (B) TEM images confirming the degradation of P3-SWNTs. Scale bar is 500 nm. (C,D) Length distribution, average length and specific standard deviation of length distribution in 1hr, 2hr and 4hr, respectively.

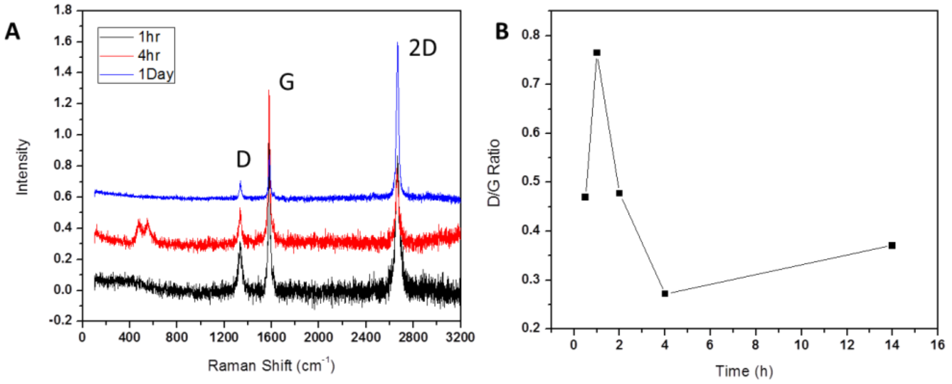

Figure 21. Raman spectra of SWNTs during NaClO oxidation
(A) Raman spectra demonstrating the defects in SWNTs during the NaClO oxidation, 1hr, 2hr and 1Day, respectively. (B) D/G ration during 14hr.

- **Functional Groups Determination and Identification of Small Oxidation Products**

In the chemical oxidation of SWNTs with NaClO, to elucidate the possible structures of the oxidation products, various methods were performed including MS, Tandem MS, NMR, HPLC, LCMS and 2D-LC. Because the relatively high concentration of salt was unavoidable, the purification was necessary prior to MS. Ideally, prior to the identification of the oxidation products by MS, they should be separated and desalted successfully using chromatography, then purified without introduction of contaminations and finally ionized and fragmented in MS and MS/MS. Different approaches were performed to obtain the optimal conditions.

The hydrophilicity and the complexity of the products make it difficult to purify and isolate a sufficient amount of substance for further analysis. As we discussed above, the degradation products should contain some or many oxygen-containing functional groups, which make them more soluble in water, rather than in organic solvents, leading to low extraction efficiency. In the chromatography, reversed phase liquid chromatography (RPLC) can hardly achieve the separation of different compounds because of the low retention interaction between the substance and the packing material. To deal with this problem, the system needs to be optimized. The typical approach would be the application of the separation based on the hydrophilicity. Strong anionic exchange (SAX)-RPLC and ion-pair chromatography were applied.

Figure 22 shows typical 2D-LC spectra and related MS spectra. In Figure 22A, separation of the products was realized in SAX. In this dimension, separation is realized based on different charges of compounds at the mobile phase pH value (pH=3 was applied after optimization). We assume the products should contain –COOH or –OH functional groups, so in relatively high pH value, they can be negatively charged, which can be retained in the column. The increasing number of charges will lead to increasing interaction and longer retention time. Then the eluents at different retention times were collected and re-injected into the second RPLC for further

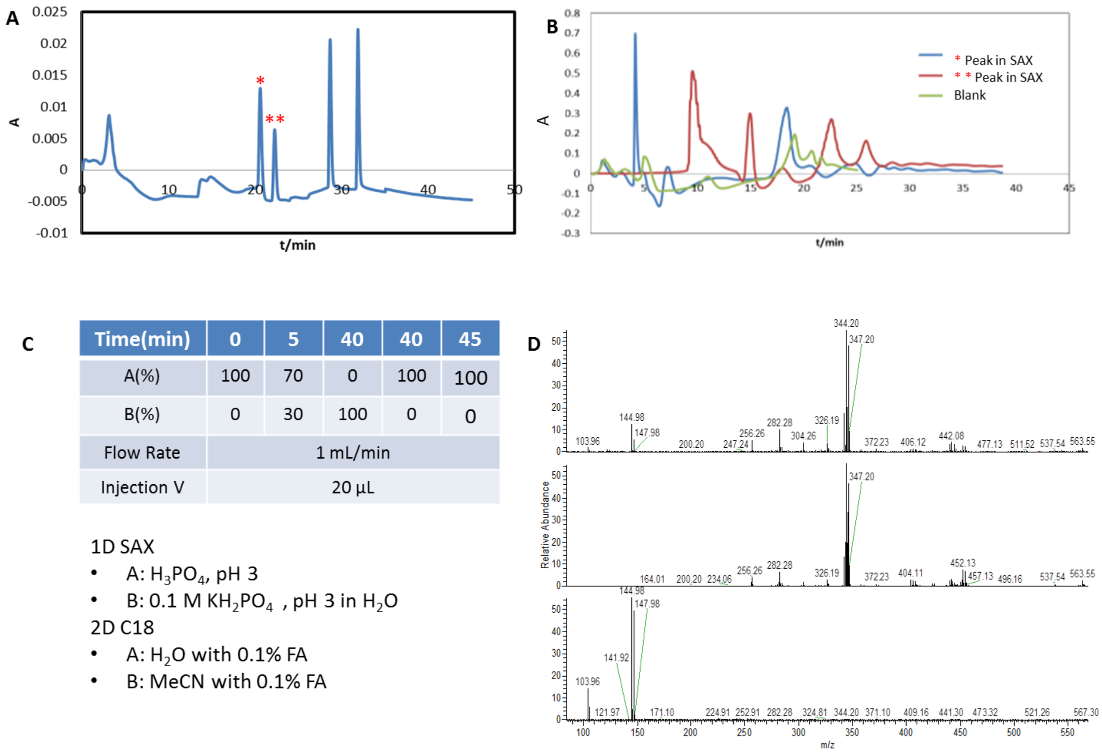

Time(min)	0	5	40	40	45
A(%)	100	70	0	100	100
B(%)	0	30	100	0	0
Flow Rate	1 mL/min				
Injection V	20 µL				

1D SAX
- A: H_3PO_4, pH 3
- B: 0.1 M KH_2PO_4 , pH 3 in H_2O

2D C18
- A: H_2O with 0.1% FA
- B: MeCN with 0.1% FA

Figure 22. Separation of Oxidation Products
(A) 1D Strong Anion Exchange (SAX) separation of oxidation product and (B) Two Peaks from 1D were collected for 2D C18 RPLC separation as labeled. (C) The same gradient program was applied in both dimension separation, while different mobile phases in accordance with the column were utilized. (D) MS of the peaks from 2D C18 column. Sample was collected from the LC system and dried with speed vac. The solid was resuspended as mentioned in Experimental Part.

*MS was done by Wentao Jiang. (Robinson Research Group) purification, mainly desalination. At this point, the eluents were collected and dried for MS spectrometry. Although the separation in the two dimensional system worked to some extent, the MS spectra at different retention times turned out to be similar and shared many peaks with the blank.

In the following research, systematic study of different purification methods prior MS were performed, including extraction with different organic solvents, solid phase extraction, Zip-tip and dialysis. In each experiment, control sample at t=0 was included. By comparing spectra of the sample and control, peaks appeared after the reaction and peaks, which intensity increased significantly, can be confirmed. Those peaks can be assigned to the oxidation products.

In extraction with ethyl acetate (Figure 23), one unique peak showed in the sample LC-MS run at retention time around 10 min (inset). The positive MS spectrum during the specific time period is depicted in Figure 23A. By comparison between this spectrum and the spectrum obtained from direct ESI-MS, several matched peaks were observed. By combination of the data, the confirmation of the presence of oxidation products was strongly supported.

So far, extraction with ethyl acetate worked the best in NaClO system, in terms of comparable results from both LC-MS and MS. More advanced separation will be performed with newly established LC-ESI-MS.

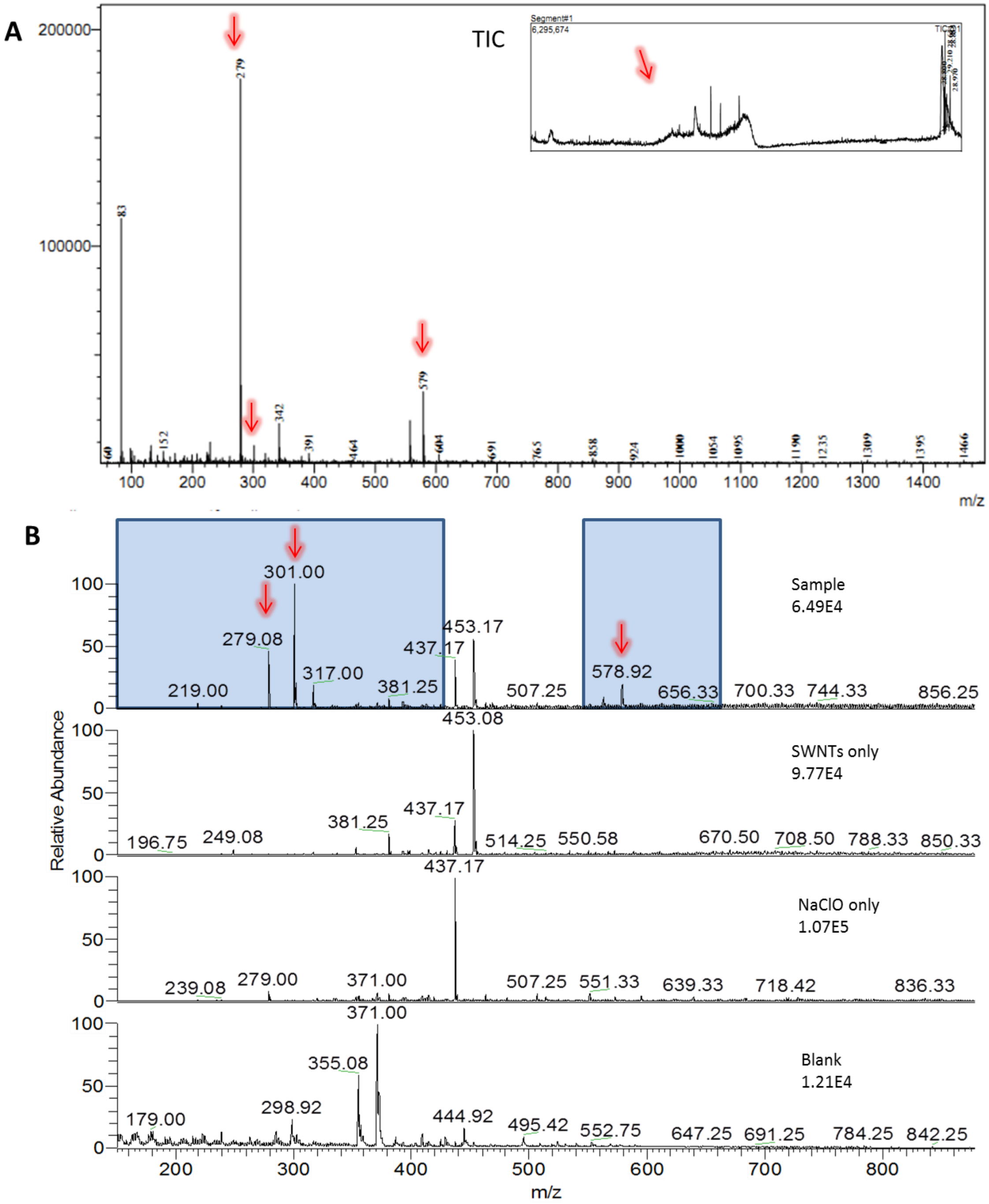

Figure 23. Comparison of MS spectra of oxidation products of SWNTs in NaClO oxidation Comparison of MS data of ethyl acetate extracted sample from HPLC-MS and direct ESI-MS (A) MS spectrum of peak at retention time around 10mins. Inset is the relevant Total Ionic Chromatography (TIC), with a unique peak shown only in sample. (B) Direct ESI-MS of sample and its related control, such as SWNTs only, NaClO only and the blank before the specific MS running. Arrows indicate the same peaks present in both spectra.

* MS was done by Wentao Jiang (Robinson Research Group)

2.4.2.2. Chemical Degradation of SWNTs with Myeloperoxidase (MPO)

- **AFM Characterization of SWNTs during MPO Enzymatic Degradation**

In previous work in our group, effectiveness of enzymatic degradation of SWNTs by MPO was studied[65,67]. All the characterizations were done in bulk, which provided the average property of the SWNTs during enzymatic degradation. To study the change of individual SWNTs, AFM was applied to monitor the degradation process of individual nanotubes immobilized on surface. Silicon chips (Figure 24) with interdigitated gold electrodes with 10 µm pitch were utilized as substrate and SWNTs were deposited via dielectrophoresis (DEP) process. Figure 24 demonstrates the chip layout and the position of markers (letters "Pitt") used for monitoring enzymatic degradation.

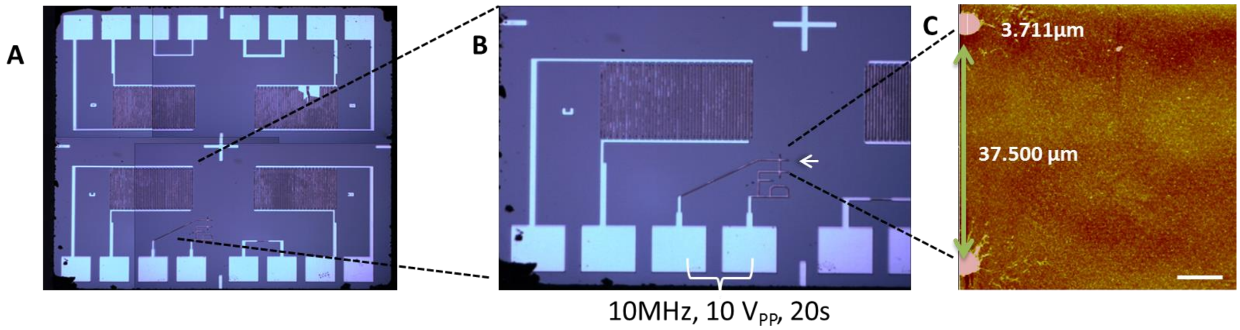

Figure 24. Chip design

Optical microscopy images of the chip. (A) Chip design. (B) Interdigitated device C at magnification of X40. Arrow points to letters "Pitt" where SWNTs were deposited. Dielectrophoresis was applied between two electrodes at frequency of 10MHz, V_{pp} of 10V for 20s.(C) AFM image of the tips of two letters "t". Scale bar is 5 µm

AFM imaging was applied to visualize the evolution of the morphology of the SWNTs at the same location during the MPO enzymatic degradation and it was conducted on the tip of the second letter “t” in “Pitt”. Silicon chip was cleaned by continuous sonication in acetone, ethanol and H_2O, 3 mins for each, and heated at 165^0C for 15mins. P3-SWNTs were deposited via DEP (10 MHz, 10 $V_{PP,}$ 20 s) and AFM image of SWNTs deposition only is shown in Figure 25 A. Then the chip was immersed in MPO solution (10 folds diluted from the stock solution) for 1h and AFM image is shown in Figure 25B. Size of MPO should be around 7.4 nm if calculated with MW as 150KDa in aqueous solution. The cross-section analysis (Figure 26), in which height of certain spots increased significantly after incubation in MPO, indicates the attachment of MPO to SWNTs .To initiate the reaction, the chip was incubated in 96-well plate at 37 ^{0}C (235 μL PB buffer+8 μL H_2O_2+7 μL NaCl). Incubation solution was replaced every 24 hrs. The reaction continued for four days and relevant AFM images are shown in Figure 25C-F.

Figure 26 demonstrates the cross-section analysis of height change along the same part of SWNTs. Although sonication was applied prior to deposition, the SWNTs were not separated thoroughly and appeared in bundles. The morphology change of SWNTs was monitored via height change. Figure 26A shows the evolution of the height along the same location of the nanotube (marked by the red line on the image) by averaging the height within the width of 10 pixels (48.8 nm) along the nanotube to reduce the error of the location selection and provide an overview of the morphology along the nanotube. If we assume that there was no end or beginning of SWNTs in the analyzed part, the height difference will result from the defects and the height increases with the incline of density of defects. Based on this assumption, discussion below will focus on two peaks labeled with red letter A and B in Figure 26A. We assume both of the peaks are resulted from defects. Before incubation with MPO at day 0, height difference between A and B was ~4 nm. After incubation in MPO solution for 1 hour, small amount of MPO molecules were deposited on the nanotube and height of an increased and the height difference increased to ~8 nm (Figure 26B). It is possible that MPO molecules attached to the A position. After reaction for 3 days, the height difference increased to ~12 nm, indicating that during this period, either A increased or B decreased or both A and B increased and decreased, respectively. We found out that the relative height between B and its adjacent peak C reduced from 4 nm to 2 nm. Possible explanation could be that the MPO tends to oxidize the nearby CNT instead of the CNT underneath it and the defects were more easily to be oxidized. Further experiments need to be done with better dispersion of SWNTs to study the change of the morphology of the carbon nanotube.

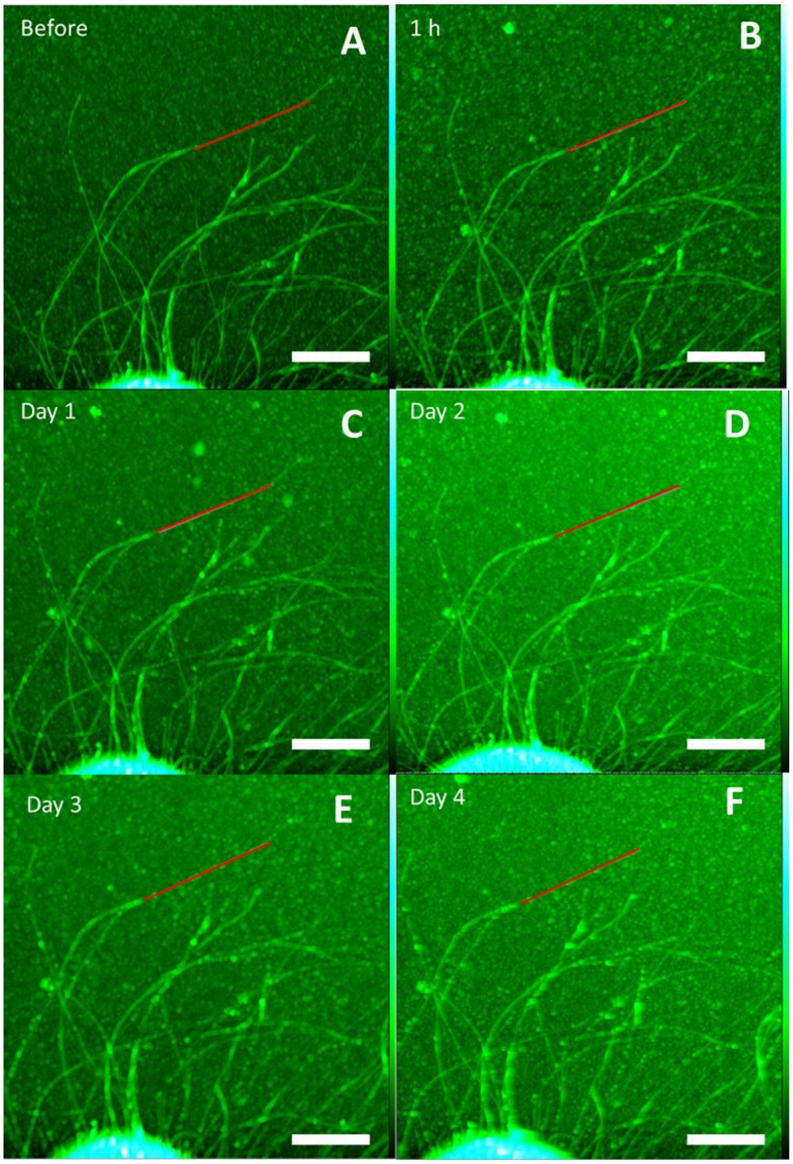

Figure 25. Monitor the evolution of MPO enzymatic degradation by AFM

AFM images of monitoring the evolution of the MPO enzymatic oxidation of SWNTs deposited. Reaction duration is as labeled. The height bars are only used to produce the best contrast. The size bars represent 1 µm.

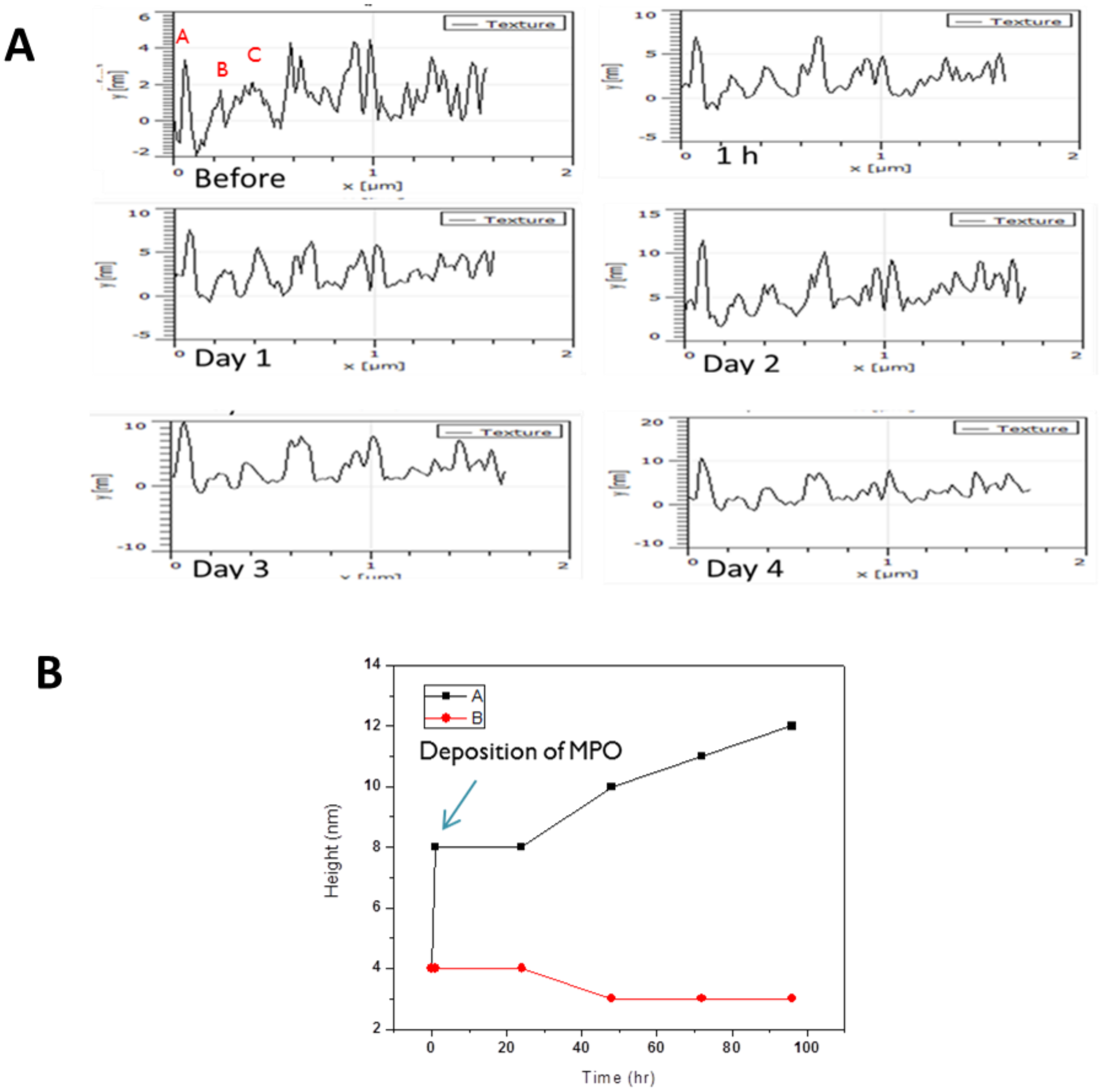

Figure 26. Height profile of SWNTs during MPO enzymatic degradation

Cross-section analysis of the SWNTs marked with the line at the same location in all images in Figure 25. (A) Section analysis representing the evolution of the average height in the width of 10 pixel (48.8 nm) along a SWNT during the oxidation. (B) Height change of two peaks from Figure 26A during the deposition and reaction process.

3. CONCLUSION AND FUTURE PLANS

3.1. Degradation Mechanism Elucidation

We have applied different analytical methods to separate, purify and identify the degradation products of different systems, including Photo-Fenton Reaction of graphene oxide, MPO enzymatic degradation and NaClO chemical oxidation of SWNTs and we successfully proposed several plausible product structures based mainly on MS and NMR spectra.

In the Photo-Fenton Reaction of graphene oxide, by combination of MS and NMR data, plausible structures were proposed successfully, and by using AFM, morphology transformation of graphene flakes to graphene quantum dots was studied. Research will be performed to learn the effectiveness of Photo-Fenton Reaction of SWNTs degradation, which theoretically can be unzipped into GO through oxidation, and the corresponding oxidation products.

In short term, for the two oxidation methods of SWNTs, further optimization is required to eliminate the ion suppression resulting from the high concentration of salt in the system. Considering the separation and purification of degradation products, LC-ESI-MS will be utilized. Different from LCMS used before, the new system can provide more accurate and precise MS information, without the introduction of further contamination. In addition, effort will be made to reduce the concentration of salt in reaction, which can still obtain the complete degradation of carbon nanomaterials.

In long term, effort will be made to elucidate the degradation mechanism in different systems, especially the enzymatic system, based on the structures proposed.

3.2. Toxicity of Degradation Products Study based on the Identified Products in Different Systems

With increasing applications of carbon nanomaterials (CNMs), toxicity of the material itself and the degradation products in biological systems and environment becomes a valid concern. At present, most of the toxicity studies only focus on the bulk property of carbon nanomaterials and the relevant conclusions are, to some extent, ambiguous. There are many possibilities about the cause of toxicity. It could result from the CNMs, residues from the synthesis process or even degradation intermediates, since CNMs can be degraded through various paths in vivo or in the environment. In addition, functionalization density is essential in evaluation of the toxicity. To better understand and eliminate the potential toxicity, in our research, systematic study of potential toxicity causes mentioned above, especially the degradation intermediates, will be performed individually.

If the structures of the degradation products were elucidated successfully, degradation mechanism for chemical oxidation and enzymatic degradation and their correlation could be illustrated. Toxicity assessment could be conducted at different stages during the degradation process in various systems. Based on the information provided by the mechanism study, condition under which the biosystem or environment exposed would no longer be ambiguous or mysterious, so that the toxicity can be evaluated effectively.

4. BIBLIOGRAPHY

(1) Ajayan, P. M., Nanotubes from carbon. *Chem. Rev.* **1999**, *99*, 1787.

(2) Iijima, S., Helical Microtubules of Graphitic Carbon. *Nature* **1991**, *354*, 56.

(3) Kroto, H. W.; Heath, J. R.; Obrien, S. C.; Curl, R. F.; Smalley, R. E., C-60 - Buckminsterfullerene. *Nature* **1985**, *318*, 162.

(4) Rao, C. N. R.; Sood, A. K.; Subrahmanyam, K. S.; Govindaraj, A., Graphene: The New Two-Dimensional Nanomaterial. *Angew. Chem. Int. Edit.* **2009**, *48*, 7752.

(5) Li, X. S.; Cai, W. W.; An, J. H.; Kim, S.; Nah, J.; Yang, D. X.; Piner, R.; Velamakanni, A.; Jung, I.; Tutuc, E.; Banerjee, S. K.; Colombo, L.; Ruoff, R. S., Large-Area Synthesis of High-Quality and Uniform Graphene Films on Copper Foils. *Science* **2009**, *324*, 1312.

(6) Hummers, W. S.; Offeman, R. E., Preparation of Graphitic Oxide. *J. Am. Chem. Soc.* **1958**, *80*, 1339.

(7) Tung, V. C.; Allen, M. J.; Yang, Y.; Kaner, R. B., High-throughput solution processing of large-scale graphene. *Nat. Nanotechnol.* **2009**, *4*, 25.

(8) Wu, Z. S.; Ren, W. C.; Gao, L. B.; Liu, B. L.; Jiang, C. B.; Cheng, H. M., Synthesis of high-quality graphene with a pre-determined number of layers. *Carbon* **2009**, *47*, 493.

(9) Subrahmanyam, K. S.; Panchakarla, L. S.; Govindaraj, A.; Rao, C. N. R., Simple Method of Preparing Graphene Flakes by an Arc-Discharge Method. *J. Phys. Chem. C* **2009**, *113*, 4257.

(10) Berger, C.; Song, Z.; Li, T.; Li, X.; Ogbazghi, A. Y.; Feng, R.; Dai, Z.; Marchenkov, A. N.; Conrad, E. H.; First, P. N.; de Heer, W. A., Ultrathin Epitaxial Graphite: 2D Electron Gas Properties and a Route toward Graphene-based Nanoelectronics. *J. Phys. Chem. B* **2004**, *108*, 19912.

(11) Berger, C.; Song, Z. M.; Li, X. B.; Wu, X. S.; Brown, N.; Naud, C.; Mayou, D.; Li, T. B.; Hass, J.; Marchenkov, A. N.; Conrad, E. H.; First, P. N.; de Heer, W. A., Electronic confinement and coherence in patterned epitaxial graphene. *Science* **2006**, *312,* 1191.

(12) Vaari, J.; Lahtinen, J.; Hautojarvi, P., The adsorption and decomposition of acetylene on clean and K-covered Co(0001). *Catal. Lett.* **1997**, *44,* 43.

(13) Ueta, H.; Saida, M.; Nakai, C.; Yamada, Y.; Sasaki, M.; Yamamoto, S., Highly oriented monolayer graphite formation on Pt(111) by a supersonic methane beam. *Surf. Sci.* **2004**, *560*, 183.

(14) Gall', N. R.; Rut'kov, E. V.; Tontegode, A. Y., Interaction of silver atoms with iridium and with a two-dimensional graphite film on iridium: Adsorption, desorption, and dissolution. *Phys. Solid State+* **2004**, *46*, 371.

(15) Reina, A.; Jia, X. T.; Ho, J.; Nezich, D.; Son, H. B.; Bulovic, V.; Dresselhaus, M. S.; Kong, J., Layer Area, Few-Layer Graphene Films on Arbitrary Substrates by Chemical Vapor Deposition. *Nano Lett.* **2009**, *9,* 3087.

(16) Bethune, D. S.; Kiang, C. H.; Devries, M. S.; Gorman, G.; Savoy, R.; Vazquez, J.; Beyers, R., Cobalt-Catalyzed Growth of Carbon Nanotubes with Single-Atomic-Layerwalls. *Nature* **1993**, *363,* 605.

(17) Iijima, S.; Ichihashi, T., Single-Shell Carbon Nanotubes of 1-Nm Diameter (Vol 363, Pg 603, 1993). *Nature* **1993**, *364*, 737.

(18) Ebbesen, T. W.; Ajayan, P. M., Large-scale Synthesis of Carbon Nanotubes. *Nature* **1992**, *358,* 220.

(19) Iijima, S.; Ichihashi, T., Single-shell Carbon Nanotubes of 1-nm. *Nature* **1993**, *363*, 603.

(20) Subramoney, S.; Ruoff, R. S.; Lorents, D. C.; Malhotra, R., Radial Single-layer Nanotubes. *Nature* **1993**, *366*, 637.

(21) Lambert, J. M.; Ajayan, P. M.; Bernier, P.; Planeix, J. M.; Brotons, V.; Coq, B.; Castaing, J., Improving Conditions towards Isolating Single-shell Carbon Nanotubes. *Chem. Phys. Lett.* **1994**, *226*, 364.

(22) Ajayan, P. M.; Lambert, J. M.; Bernier, P.; Barbedette, L.; Colliex, C.; Planeix, J. M., Growth Morphologies during Cobalt-catalyzed Single-shell Carbon Nanotube Synthesis. *Chem. Phys. Lett.* **1993**, *215*, 509.

(23) Journet, C.; Maser, W. K.; Bernier, P.; Loiseau, A.; delaChapelle, M. L.; Lefrant, S.; Deniard, P.; Lee, R.; Fischer, J. E., Large-scale production of single-walled carbon nanotubes by the electric-arc technique. *Nature* **1997**, *388*, 756.

(24) Saito, Y.; Tani, Y.; Miyagawa, N.; Mitsushima, K.; Kasuya, A.; Nishina, Y., High yield of single-wall carbon nanotubes by arc discharge using Rh-Pt mixed catalysts. *Chem. Phys. Lett.* **1998**, *294*, 593.

(25) Huang, H. J.; Kajiura, H.; Tsutsui, S.; Hirano, Y.; Miyakoshi, M.; Yamada, A.; Ata, M., Large-scale rooted growth of aligned super bundles of single-walled carbon nanotubes using a directed arc plasma method. *Chem. Phys. Lett.* **2001**, *343*, 7.

(26) Guo, T.; Nikolaev, P.; Rinzler, A. G.; Tomanek, D.; Colbert, D. T.; Smalley, R. E., Self-assembly of Tubular Fullerenes. *J. Phys. Chem.* **1995**, *99*, 10694.

(27) Thess, A.; Lee, R.; Nikolaev, P.; Dai, H. J.; Petit, P.; Robert, J.; Xu, C. H.; Lee, Y. H.; Kim, S. G.; Rinzler, A. G.; Colbert, D. T.; Scuseria, G. E.; Tomanek, D.; Fischer, J. E.; Smalley, R. E., Crystalline ropes of metallic carbon nanotubes. *Science* **1996**, *273*, 483.

(28) Inami, N.; Mohamed, M. A.; Shikoh, E.; Fujiwara, A., Synthesis-condition dependence of carbon nanotube growth by alcohol catalytic chemical vapor deposition method. *Sci. Technol. Adv. Mater.* **2007**, *8*, 292.

(29) Ishigami, N.; Ago, H.; Imamoto, K.; Tsuji, M.; Iakoubovskii, K.; Minami, N., Crystal plane dependent growth of aligned single-walled carbon nanotubes on sapphire. *J. Am. Chem. Soc.* **2008**, *130*, 9918.

(30) Naha, S.; Puri, I. K., A model for catalytic growth of carbon nanotubes. *J. Phys. D-Appl. Phys.* **2008**, *41*.

(31) Baker, R. T. K.; Barber, M. A.; Waite, R. J.; Harris, P. S.; Feates, F. S., Nucleation and Growth of Carbon Deposits from Nickel Catalyzed Decomposition of Acetylene. *J. Catal.* **1972**, *26*, 51.

(32) Baker, R. T. K.; Chludzinski, J. J., Filamentous Carbon Growth on Nickel-iron Surface – the Effect of Various Oxide Additives. *J. Catal.* **1980**, *64*, 464.

(33) Baker, R. T. K.; Harris, P. S.; Thomas, R. B.; Waite, R. J., Formation of Filamentous Carbon From Iron, Cobalt and Chromium Catalyzed Decomposition of Acetylene. *J. Catal.* **1973**, *30*, 86.

(34) Tibbetts, G. G., Carbon – fibers Produced by Pyrolysis of Natural-gas in Stainless – Steel Tubes. *Appl. Phys. Lett.* **1983**, *42*, 666.

(35) Blake, R.; Gun'ko, Y. K.; Coleman, J.; Cadek, M.; Fonseca, A.; Nagy, J. B.; Blau, W. J., A generic organometallic approach toward ultra-strong carbon nanotube polymer composites. *J. Am. Chem. Soc.* **2004**, *126*, 10226.

(36) Burg, B. R.; Poulikakos, D., Large-scale integration of single-walled carbon nanotubes and graphene into sensors and devices using dielectrophoresis: A review. *J. Mater. Res.* **2011**, *26*, 1561.

(37) Chen, Z.; Zhang, X. B.; Yang, R. H.; Zhu, Z.; Chen, Y.; Tan, W. H., Single-walled carbon nanotubes as optical materials for biosensing. *Nanoscale* **2011**, *3*, 1949.

(38) Wu, H. C.; Chang, X. L.; Liu, L.; Zhao, F.; Zhao, Y. L., Chemistry of carbon nanotubes in biomedical applications. *J. Mater. Chem.* **2010**, *20*, 1036.

(39) Wei, Z.; Kondratenko, M.; Dao, L. H.; Perepichka, D. F., Rectifying diodes from asymmetrically functionalized single-wall carbon nanotubes. *J. Am. Chem. Soc.* **2006**, *128*, 3134.

(40) Rastogi, R.; Kaushal, R.; Tripathi, S. K.; Sharma, A. L.; Kaur, I.; Bharadwaj, L. M., Comparative study of carbon nanotube dispersion using surfactants. *J. Colloid. Interf. Sci.* **2008**, *328*, 421.

(41) Hwang, G. L.; Hwang, K. C., Carbon nanotube reinforced ceramics. *J. Mater. Chem.* **2001**, *11*, 1722.

(42) Fenton, H. J. H., LXXIII.-Oxidation of tartaric acid in presence of iron. *J. Chem. Soc., Transactions* **1894**, *65*, 899.

(43) Walling, C., FENTONS REAGENT REVISITED. *Acc. Chem. Res.* **1975**, *8*, 125.

(44) Bauer, R.; Fallmann, H., The Photo-Fenton oxidation - A cheap and efficient wastewater treatment method. *Rev. Sci. Instrum.* **1997**, *23*, 341.

(45) Ikehata, K.; El-Din, M. G.,Aqueous pesticide degradation by hydrogen peroxide/ultraviolet irradiation and Fenton-type advanced oxidation processes: a review. *J. Environ. Eng. Sci.* **2006**, *5*, 81.

(46) Lee, S.; Oh, J.; Park, Y., Degradation of phenol with fenton-like treatment by using heterogeneous catalyst (modified iron oxide) and hydrogen peroxide. *B. Kor. Chem. Soc.* **2006**, *27*, 489.

(47) Palmroth, M. R.; Langwaldt, J. H.; Aunola, T. A.; Goi, A.; Puhakka, J. A.; Tuhkanen, T. A., Treatment of PAH-contaminated soil by combination of Fenton's reaction and biodegradation. *J. Chem. Technol. Biot.* **2006**, *81*, 598.

(48) Barreiro, J. C.; Capelato, M. D.; Martin-Neto, L.; Bruun Hansen, H. C., Oxidative decomposition of atrazine by a Fenton-like reaction in a H_2O_2/ferrihydrite system. *Water Res.* **2007**, *41*, 55.

(49) Jonsson, S.; Persson, Y.; Frankki, S.; van Bavel, B.; Lundstedt, S.; Haglund, P.; Tysklind, M., Degradation of polycyclic aromatic hydrocarbons (PAHs) in contaminated soils by Fenton's reagent: a multivariate evaluation of the importance of soil characteristics and PAH properties. *J. Hazard. Mater.* **2007**, *149*, 86.

(50) Liao, Q.; Sun, J.; Gao, L., Degradation of phenol by heterogeneous Fenton reaction using multi-walled carbon nanotube supported Fe_2O_3 Catalysts. *Colloid Surface A* **2009**, *345,* 95.

(50) Liao, Q.; Sun, J.; Gao, L., Degradation of phenol by heterogeneous Fenton reaction using multi-walled carbon nanotube supported Fe(2)O(3) Catalysts. *Colloid Surface A* **2009**, *345*, 95.

(51) Ai, Z. H.; Xiao, H. Y.; Mei, T.; Liu, J.; Zhang, L. Z.; Deng, K. J.; Qiu, J. R., Electro-fenton degradation of rhodamine B based on a composite cathode of Cu2O nanocubes and carbon nanotubes. *J. Phys. Chem. C* **2008**, *112*, 11929.

(52) Zhang, K.; Meng, Z.; Oh, W., Degradation of Rhodamine B by Fe-Carbon Nanotubes/TiO2 Composites under UV Light in Aerated Solution. *Chinese J. Catal.* **2010**, *31*, 751.

(53) Zhao, B. X.; Li, X. Z.; Wang, P., 2,4-dichlorophenol degradation by an integrated process: Photoelectrocatalytic oxidation and E-Fenton oxidation. *Photochem. Photobiol.* **2007**, *83*, 642.

(54) Fan, C. L.; Li, W.; Li, X.; Zhao, S. J.; Zhang, L.; Mo, Y. J.; Cheng, R. M., Efficient photo-assisted Fenton oxidation treatment of multi-waited carbon nanotubes. *Chinese Sci. Bull.* **2007**, *52*, 2054.

(55) Zhou, X.; Zhang, Y.; Wang, C.; Wu, X.; Yang, Y.; Zheng, B.; Wu, H.; Guo, S.; Zhang, J., Photo-fenton reaction of graphene oxide: a new strategy to prepare graphene quantum dots for DNA cleavage. *Acs Nano* **2012**, *6*, 6592.

(56) Ouyang, M.; Huang, J. L.; Lieber, C. M., Fundamental electronic properties and applications of single-walled carbon nanotubes. *Acc. Chem. Res.* **2002**, *35*, 1018.

(57) Kagan, V. E.; Tyurina, Y. Y.; Tyurin, V. A.; Konduru, N. V.; Potapovich, A. I.; Osipov, A. N.; Kisin, E. R.; Schwegler-Berry, D.; Mercer, R.; Castranova, V.; Shvedova, A. A., Direct and indirect effects of single walled carbon nanotubes on RAW 264.7 macrophages: Role of iron. *Toxicol. Lett.* **2006**, *165*, 88.

(58) Kisin, E. R.; Murray, A. R.; Keane, M. J.; Shi, X.-C.; Schwegler-Berry, D.; Gorelik, O.; Arepalli, S.; Castranova, V.; Wallace, W. E.; Kagan, V. E.; Shvedova, A. A., Single-walled carbon nanotubes: Geno- and cytotoxic effects in lung fibroblast V79 cells. *J. Toxicol. Env. Heal.* **2007**, *70*, 2071.

(59) Kuznetsova, A.; Popova, I.; Yates, J. T.; Bronikowski, M. J.; Huffman, C. B.; Liu, J.; Smalley, R. E.; Hwu, H. H.; Chen, J. G. G., Oxygen-containing functional groups on single-wall carbon nanotubes: NEXAFS and vibrational spectroscopic studies. *J. Am. Chem. Soc.* **2001**, *123*, 10699.

(60) Panasenko, O. M.; Chekanov, A. V.; Arnhold, J.; Sergienko, V. I.; Osipov, A. N.; Vladimirov, Y. A., Generation of free radicals during decomposition of hydroperoxide in the presence of myeloperoxidase or activated neutrophils. *Biochemistry-Moscow* **2005**, *70*, 998.

(61) Allen, B. L.; Kichambare, P. D.; Gou, P.; Vlasova, I. I.; Kapralov, A. A.; Konduru, N.; Kagan, V. E.; Star, A., Biodegradation of Single-Walled Carbon Nanotubes through Enzymatic Catalysis. *Nano Lett.* **2008**, *8*, 3899.

(62) Allen, B. L.; Kotchey, G. P.; Chen, Y. N.; Yanamala, N. V. K.; Klein-Seetharaman, J.; Kagan, V. E.; Star, A., Mechanistic Investigations of Horseradish Peroxidase-Catalyzed Degradation of Single-Walled Carbon Nanotubes. *J. Am. Chem. Soc.* **2009**, *131*, 17194.

(63) Osorio, A. G.; Silveira, I. C. L.; Bueno, V. L.; Bergmann, C. P., $H_2SO_4/HNO_3/HCl$-Functionalization and its effect on dispersion of carbon nanotubes in aqueous media. *Appl. Surf. Sci.* **2008**, *255*, 2485.

(64) Vlasova, I. I.; Sokolov, A. V.; Chekanov, A. V.; Kostevich, V. A.; Vasilyev, V. B., Myeloperoxidase-Induced Biodegradation of Single-Walled Carbon Nanotubes Is Mediated by Hypochlorite. *Russ. J. Bioorg. Chem.* **2011**, *37*, 453.

(65) Kagan, V. E.; Konduru, N. V.; Feng, W. H.; Allen, B. L.; Conroy, J.; Volkov, Y.; Vlasova, II; Belikova, N. A.; Yanamala, N.; Kapralov, A.; Tyurina, Y. Y.; Shi, J. W.; Kisin, E. R.; Murray, A. R.; Franks, J.; Stolz, D.; Gou, P. P.; Klein-Seetharaman, J.;

Fadeel, B.; Star, A.; Shvedova, A. A., Carbon nanotubes degraded by neutrophil myeloperoxidase induce less pulmonary inflammation. *Nat. Nanotechnol.* **2010**, *5*, 354.

(66) Zhao, Y.; Allen, B. L.; Star, A., Enzymatic Degradation of Multiwalled Carbon Nanotubes. *J. Phys. Chem. A* **2011**, *115*, 9536.

(67) Kotchey, G. P.; Hasan, S. A.; Kapralov, A. A.; Ha, S. H.; Kim, K.; Shvedova, A. A.; Kagan, V. E.; Star, A., A natural vanishing act: the enzyme-catalyzed degradation of carbon nanomaterials. *Acc. Chem. Res.* **2012**, *45*, 1770.

(68) Kotchey, G. P.; Allen, B. L.; Vedala, H.; Yanamala, N.; Kapralov, A. A.; Tyurina, Y. Y.; Klein-Seetharaman, J.; Kagan, V. E.; Star, A., The Enzymatic Oxidation of Graphene Oxide. *Acs Nano* **2011**, *5*, 2098.

(69) Ros, T. G.; van Dillen, A. J.; Geus, J. W.; Koningsberger, D. C., Surface oxidation of carbon nanofibres. *Chem-Eur. J.* **2002**, *8*, 1151.

(70) Su, F. S.; Lu, C. Y.; Hu, S. K., Adsorption of benzene, toluene, ethylbenzene and p-xylene by NaOCl-oxidized carbon nanotubes. *Colloid Surface A* **2010**, *353*, 83.

(71) Toebes, M. L.; van Heeswijk, E. M. P.; Bitter, J. H.; van Dillen, A. J.; de Jong, K. P., The influence of oxidation on the texture and the number of oxygen-containing surface groups of carbon nanofibers. *Carbon* **2004**, *42*, 307.

(72) Lessig, J.; Spalteholz, H.; Reibetanz, U.; Salavei, P.; Fischlechner, M.; Glander, H.-J.; Arnhold, J., Myeloperoxidase binds to non-vital spermatozoa on phosphatidylserine epitopes. *Apoptosis : an international journal on programmed cell death* **2007**, *12*, 1803.

(73) http://en.wikipedia.org/wiki/Mikhail_Tsvet. (Accessed on January 2013)

(74) http://en.wikipedia.org/wiki/Liquid_chromatography. (Accessed on January 2013)

(75) http://en.wikipedia.org/wiki/Chromatography. (Accessed on January 2013)

(76) Meyer, V. R. *Practical High-Performance Liquid Chromatography*; Fifth ed.; John Wiley and Sons, Ltd.: Padstow, 2010.

(77) http://www.files.chem.vt.edu/chem-ed/sep/lc/hplc.html. (Accessed on January 2013)

(78) B.E. Lendi and V.R. Meyer, L. G. E., 18, 156 (2005). *For diode-array detectors*, Section 6.10.

(79) Harold F. Walton, R. D. R. *Ion Exchange in Analytical Chemistry*; CRC Press, Inc.: Boca Raton, 1990.

(80) Erickson, B. E., Electrochemical detectors for liquid chromatography. *Anal. Chem.* **2000**, *72*, 353A.

(81) Lee, M. S.; Kerns, E. H., LC/MS applications in drug development. *Mass Spectrom. Rev.* **1999**, *18*, 187.

(82) Jemal, M., High-throughput quantitative bioanalysis by LC/MS/MS. *Biomed. Chromatogr* **2000**, *14*, 422.

(83) Alder, L.; Greulich, K.; Kempe, G.; Vieth, B.,Residue analysis of 500 high priority pesticides: Better by GC-MS or LC-MS/MS? *Mass Spectrom.Rev.* **2006**, *25*, 838.

(84) Cole, R. B. *Electrospray and MALDI Mass Spectrometry*; 2nd ed.; John Wiley & Sons, Inc.: Hoboken, 2010.

(85) Cech, N. B.; Enke, C. G., Practical implications of some recent studies in electrospray ionization fundamentals. *Mass Spectrom. Rev.* **2001**, *20*, 362.

(86) http://www.magnet.fsu.edu/education/tutorials/tools/ionization_maldi.html (Accessed on January 2013)

(87) Olsen, J. V.; Schwartz, J. C.; Griep-Raming, J.; Nielsen, M. L.; Damoc, E.; Denisov, E.; Lange, O.; Remes, P.; Taylor, D.; Splendore, M.; Wouters, E. R.; Senko, M.; Makarov,

A.; Mann, M.; Horning, S., A Dual Pressure Linear Ion Trap Orbitrap Instrument with Very High Sequencing Speed. *Mol.Cell. Proteomics* **2009**, *8*, 2759.

(88) March, R. E., An Introduction to Quadrupole Ion Trap Mass Spectrometry. *Journal of Mass Spectrom.* **1997**, *32*, 351.

(89) Perry, R. H.; Cooks, R. G.; Noll, R. J., Orbitrap mass spectrometry: instrumentation, ion motion and applications. *Mass Spectrom. Rev.* **2008**, *27*, 661.

(90) Hu, Q.; Noll, R. J.; Li, H.; Makarov, A.; Hardman, M.; Graham Cooks, R.,The Orbitrap: a new mass spectrometer. *J. Mass Spectrom.***2005**, *40*, 430.

(91) Makarov, A., Electrostatic Axially Harmonic Orbital Trapping: A High-Performance Technique of Mass Analysis. *Anal. Chem.* **2000**, *72*, 1156.

(92) Keeler, J. *Understanding NMR Spectroscopy*; 2nd ed.; John Wiley & Sons, Inc.: Padstow, 2010.